

# Magnetospheric truncation of an accretion disk around the unique X-ray pulsar GRO J1744–28

Master's Thesis  
University of Turku  
Department of Physics and Astronomy  
Astronomy  
2017  
Juhani Mönkkönen  
Supervised by:  
Sergey Tsygankov

The originality of this thesis has been checked in accordance with the University of Turku quality assurance system using the Turnitin OriginalityCheck service.

UNIVERSITY OF TURKU  
Department of Physics and Astronomy

MÖNKKÖNEN, JUHANI: Magnetospheric truncation of an accretion disk around the  
unique X-ray pulsar GRO J1744–28

Master's thesis, 50 pages  
Astronomy  
May 2017

---

Neutron stars are very massive yet compact objects, where both quantum mechanical and relativistic effects play a role. Many of them have magnetic fields which are many orders of magnitude stronger than what mankind can achieve in laboratories. In systems where a neutron star accretes matter from its binary companion, the magnetic fields affect the accretion process. If the accreted matter forms an accretion disk around the neutron star, the disk will be truncated and the matter guided onto the magnetic poles by the magnetic field. How this truncation happens and how the magnetic field shapes the resulting X-ray emission, depend on complex interactions between matter and radiation in these extreme fields. Thus observations of these nature's high-energy laboratories are crucial to the development of up-to-date physical models.

In my thesis, I examined observations of a unique accreting highly magnetized neutron star GRO J1744–28, also known as Bursting Pulsar. The pulsar reaches very high luminosities, at which its accretion disk might have a radiation pressure dominated inner zone, a feature which hasn't been directly observed in any other accreting X-ray pulsar. This could explain the rare type II bursts which are seen in this source and have been suggested to arise in a radiation-dominated accretion disk.

Random fluctuations are present in light curves of every accreting X-ray source and they are shaped at different timescales by various stochastic processes in the accretion disk. A natural way to inspect the fluctuations is a power density spectrum, which is a Fourier transform of the light curve data from time domain into frequency domain. In the present thesis, this method of timing analysis was utilized extensively and power density spectra were used for probing the conditions in the accretion disk at different luminosities. Theoretical framework was provided by the 'perturbation propagation' model, which can explain how the shape of power spectra depend on the size and structure of the accretion disk. According to the perturbation propagation model, we should see a break in the power spectrum at high frequencies, where the break frequency corresponds to the Keplerian orbital frequency of the inner disk edge. Using the break frequencies in power spectra, we can then deduce the size of the magnetosphere at different luminosities.

The observed dependency of the break frequency on the luminosity is discussed in the frame of this perturbation propagation model and the dependency is shown to be inconsistent with a standard gas-pressure dominated inner disk at high luminosities. The shape of the power spectrum is calculated for an accretion disk which has a radiation-pressure dominated inner zone and compared to the data. We show that the data is consistent with the picture that the inner accretion disk is radiation pressure dominated.

*keywords : Neutron stars, Accreting X – ray pulsars, Power density spectra*

## **Acknowledgements**

I would like to thank my supervisor Sergey Tsygankov for all the support, advice and learning possibilities I got when working with the challenging source GRO J1744–28, and for encouraging me to question and ask questions. I'm also highly thankful of all the considerations and work done by Alexander Mushtukov, helping me to truly find out what I found. A great thank goes also to professor Juri Poutanen for supporting my process. I'm also thankful for my colleagues working in the astrophysics research group for all the discussions and helpful comments. And without my family, friends and especially my boyfriend Niko, I never would have even started and finished this work. So thank you all for the support and encouragement and belief in me and my abilities.

# Contents

<b>Introduction</b>	<b>1</b>
<b>1 Accreting highly magnetized neutron stars</b>	<b>3</b>
<b>2 Unique X-ray pulsar GRO J1744–28</b>	<b>6</b>
<b>3 Disk-magnetosphere interaction</b>	<b>10</b>
3.1 Accretion disk . . . . .	10
3.2 Magnetospheric truncation . . . . .	13
3.3 Accretion disk as the source of variability in flux . . . . .	20
3.4 Instabilities and type II bursts . . . . .	23
<b>4 Methods</b>	<b>26</b>
4.1 Data reduction . . . . .	26
4.1.1 Rossi X-ray Timing Explorer . . . . .	26
4.1.2 Timing analysis . . . . .	27
4.1.3 Spectral analysis . . . . .	28
4.2 Power density spectra . . . . .	30
<b>5 Results and discussion</b>	<b>31</b>
5.1 Bursts . . . . .	31
5.2 Pulse profiles . . . . .	33
5.3 Power density spectra in different luminosities . . . . .	34
5.3.1 Shape . . . . .	34
5.3.2 Break frequency and QPOs . . . . .	39
5.3.3 Inner radius . . . . .	42
<b>6 Summary</b>	<b>45</b>
<b>References</b>	<b>47</b>

## Introduction

A neutron star (NS) is the very compact remnant of a massive star, and in it, both general relativistic and quantum mechanical effects play a strong role in various physical processes. In a binary system, where two stars orbit around each other, one of the stars may evolve faster than its companion and become a NS. In these binary systems, mass transfer from the companion onto the NS may be possible. Accretion from a low-mass companion will proceed via an accretion disk, a structure where matter (in plasma state) orbits the star in a nearly Keplerian way until it is accreted onto the NS. In the disk and on the NS surface, initial potential energy of accreted matter will be converted into kinetic energy and further into thermal energy, which will then be dissipated and radiated in a wide spectral energy range, from infrared to X-rays. NSs are very efficient in this process, and at least 10 per cent of the rest mass of accreted matter is converted into radiation.

When a NS is born, the initial magnetic field will be amplified by many orders of magnitude. Field strengths varying from  $10^8$  G to  $10^{15}$  G have been observed in these sources. With these extremely high magnetic field strengths, which far exceed the values achieved by mankind in laboratories, NSs are Nature's own laboratories where the fundamental theories of physics can be tested. Thus diverse high-resolution observations of highly magnetized NSs are very important.

In strong magnetic fields, the motion of charged particles is confined in transverse direction with respect to the field lines. In a highly magnetized NS, the accretion disk will thus be truncated at the radius where the stresses of disk plasma and NS magnetic field become equal. The disk becomes truncated as the matter is bound to the magnetic field lines and guided from the disk plane onto the NS magnetic poles. Rest of the potential and kinetic energy is then radiated away above the NS magnetic poles. Since the NS magnetic axis is typically inclined with respect to the NS rotational axis (just as in the case of Earth's magnetic field) accreting NSs can appear as X-ray pulsars with a periodically modulated X-ray flux.

The basic picture for the behaviour of the magnetospheric truncation is that when the mass accretion rate increases, the gas (and radiation) pressure in the accretion disk also increase and are able to push the inner radius further into the NS magnetosphere [1]. Especially, the predictions for how the inner radius depends on the mass accretion rate offer a way to examine the disk physics. In reality, the magnetospheric truncation is still a poorly understood process and various models with different predictions have been proposed for the interface between an accretion disk and a magnetosphere (see [2] for a review). Simulations are CPU-intensive and may produce numerical artefacts (see, e.g. [3]) so observations of accreting X-ray pulsars offer another way to find out what are the conditions and physics in the extreme environment.

The inner disk radius can be determined from model fits to source spectra, but the models have many parameters and assumptions behind their interpretation (see, e.g. [1, 4] for theory and [5] for observational application). Examining the variation in the light curve through power density spectra (PDS) offers an independent way. In the light of perturbation propagation model, the conditions in the accretion disk can be inferred from PDS [6].

GRO J1744–28 is a unique X-ray pulsar which is the only source known to show both X-ray pulsations and recurring type II X-ray bursts [7]. The source has been observed in three outbursts, in which the source reached very high luminosities. The magnetic field strength for the source has been estimated to be around  $10^{11}$  G. At this magnetic field strength, the inner accretion disk might be radiation pressure dominated (RPD) during the outbursts. This would be the first time a RPD region is observed in any X-ray pulsar accretion disk. Examining the PDS of this source can be used to determine whether the inner disk is in a RPD state, thus potentially revealing more about the physics at the disk-magnetosphere interface.

# 1 Accreting highly magnetized neutron stars

NSs are the dense end result of stellar evolution. The cores of stars more massive than 8 solar masses collapse when the fusion processes have turned the core matter from initial cosmic mixture into iron and further fusion is not energetically possible. For a core with a mass exceeding the Chandrasekhar limit of 1.4 solar masses, electron degeneracy will not provide enough pressure to resist the self-gravitational collapse after the energy production has halted. The core then collapses and causes a supernova explosion, when most of the core matter becomes neutrons through electron capture in nuclei and neutrinos forming in the process drive the shock which expels the outer stellar matter falling onto the core. [8]

The resulting NSs are very compact: they have masses around 1.4 solar masses but radii only of the order of 10 km ( $10^6$  cm). We adopt these characteristic values in the present thesis. The length scales can be given using the gravitational radius  $R_G = GM/c^2$ , where  $G$  is the gravitational constant,  $M$  is the NS mass and  $c$  is the speed of light. This can be simplified to  $1.5 m$  km where  $m$  is the NS mass in units of solar masses. The core densities in a NS exceed the nuclear densities because it is the neutron degeneracy pressure that is counteracting the gravitational pull of the NS matter. The formation process of a NS amplifies the initial stellar magnetic field so that the NS magnetic field strengths has been measured and estimated to vary from  $10^8$  G to  $10^{15}$  G. [9]

In strong magnetic fields, the circular motion of charged particles is quantized: radiation quanta can be absorbed and emitted by particles at the Landau energy levels of electrons with separation  $\hbar e/m_e c$  where  $\hbar$  is the reduced Planck constant,  $e$  is the elementary charge,  $m_e$  is the electron rest mass and  $c$  is the speed of light. Emission and absorption of radiation by particles with different velocities will scatter photons with energies close to the Landau energy levels and cause an absorption line in the energy spectrum. The central energy of the line is related to the magnetic field strength as

$$E_{\text{cycl}} = 11.6 B_{12} (1 + z)^{-1} \text{keV}, \quad (1)$$

where  $B_{12}$  is the magnetic field strength in units of  $10^{12}$  G and  $z$  is the relativistic gravitational redshift related to NS parameters as  $1 + z = (1 - 2GM/c^2R)^{-1/2}$ . This means that the measured cyclotron lines in energy spectra of highly magnetized NSs can be used to find their magnetic field strengths. Since the dipole component of the magnetic field decreases as  $R^{-3}$ , it is more convenient to use the magnetic dipole moment  $\mu = BR^3$  where  $R$  is the distance at which the magnetic field strength is measured.

If one of the components in a binary system becomes a NS, mass transfer from its companion star onto the NS is possible. Depending on the system parameters, such as the semi-major axis and the mass ratio, accretion may proceed via a stellar wind or an accretion disk and the situation can change over time through mass transfer, magnetic braking and gravitational radiation [10]. In a rotating binary system, the gravitational potential has an additional term from the centrifugal force. This Roche potential has a specific shape, which is possible to derive analytically. A cut through the system in the plane of rotation shows an equipotential curve which resembles the figure eight enclosing the stars in its loops. Roche lobes are such tear-drop shaped volumes around the stars, inside which the free-falling matter is gravitationally bound to the central star. If the companion star reaches the border of its Roche lobe, for example, when it is in a late stage of its evolution and its envelope has expanded, Roche lobe overflow allows matter to flow through the Lagrange 1 point of the binary, after which an accretion disk will form around the NS (see Figure 1). [11]

Accreting magnetized NSs can appear in binary systems which can be roughly divided into two categories: High-mass X-ray binaries (HMXB) have a massive companion star (mass typically greater than  $6 - 7M_{\odot}$ ) of O or B spectral class, and due to fast evolution of massive stars, the systems are young and often located in the Galactic Disk. The companion is bright in optical and has strong winds so accretion can proceed both through wind and accretion disk. The NS in HMXB typically has a magnetic field of  $B \gtrsim 10^{11}$  G. Low-mass X-ray binaries (LMXB) host a less massive (mass typically below  $1 - 2M_{\odot}$ ), main

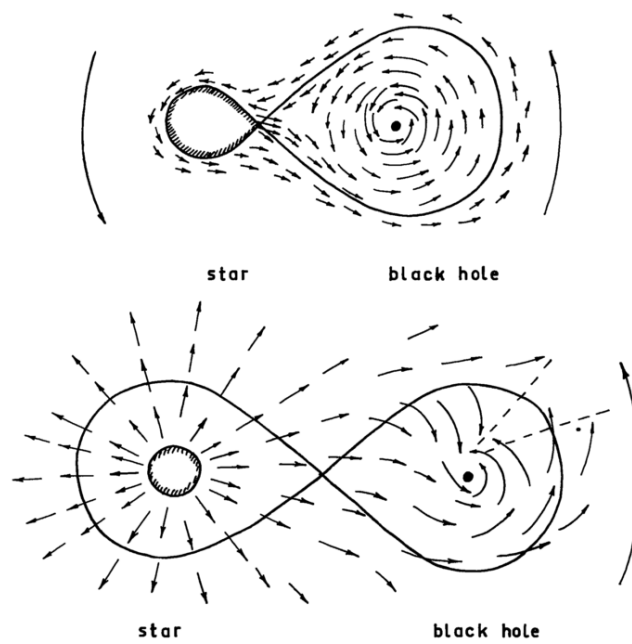


Figure 1. The basic picture of accretion onto a compact object for both Roche lobe overflow and wind capture (upper and lower, respectively) [11]. In Roche lobe overflow, an accretion disk forms, while in wind capture, the formation of a shock wave enables accretion. If the compact object is a NS, the picture changes close to the magnetosphere [1].

sequence or evolved companion thus being found mostly in the Galactic Bulge. Accretion in LMXBs happens when the companion star fills its Roche lobe and an accretion disk forms. Since the systems are usually very old, the strength of NS magnetic field is lower, ranging from  $10^8$  G to  $10^{10}$  G. [12]

## 2 Unique X-ray pulsar GRO J1744–28

GRO J1744–28 was discovered in December 1995 with the Burst and Transient Source Experiment (BATSE) on *Compton Gamma-Ray Observatory* when frequent, spectrally hard bursts were observed from the Galactic Center [13]. The source was suspected to be an accreting NS with unique type II bursts [14]. Persistent pulsations of 467 milliseconds and subsequent spin-up confirmed that the source indeed is a NS accreting from a low-mass companion star via an accretion disk, and the binary period was measured to be 11.8 days [15]. The source was the first to show both type II bursts and pulsations so it was given the nickname *Bursting Pulsar*. In its outbursts, GRO J1744–28 reached super-Eddington luminosities [16].

Type II bursts are seen in few sources, mainly in *Bursting Pulsar* and *Rapid Burster*, but the sources have different bursting behaviour. Early during the first outburst of *Bursting Pulsar*, the type II bursts had shorter intervals ( $\sim 3$  minutes), and unlike in *Rapid Burster*, there was no significant correlation between burst fluence (flux integrated in time) and time to the following burst [14]. Giles *et al.* (1996) [17] reported that the bursts occurred with a mean interval of half an hour and were followed by flux deficits (depressions or dips) during which the flux recovered back to pre-burst flux level. They also mentioned that when luminosity decreased, the recovery periods started to have more variations in shape and later the post-burst dips disappeared entirely. In lower luminosities, some bursting occurred but the mechanisms might have been different [18]. More of the bursting behaviour and its indications for the disk structure are discussed in section 5.1.

Type II bursts are thought to result from some sort of accretion instabilities. Cannizzo

(1996) [19] successfully modelled the type II bursts of GRO J1744–28 as resulting from a Lightman-Eardley instability, which is a surface density instability arising in a RPD accretion disk [20]. According to the model, the inner radius of the disk should be located in the RPD region above certain luminosity. At high luminosities and mass accretion rates of GRO J1744–28, the inner accretion disk is indeed expected to become RPD (see section 3.2). This served as a motivation to conduct an independent examination of the inner disk and verify the appearance of a RPD region.

GRO J1744–28 was observed with the Rossi X-Ray Timing Explorer (*RXTE*) more or less regularly from January 1996 to November 1997, which corresponds to modified Julian date (MJD) from 50110 to 50770. During this time the source showed two bright outbursts with a solar exclusion in between (see Figure 2). Most of the observations were done with either  $244 \mu\text{s}$  or  $122 \mu\text{s}$  time resolution. This high time resolution data was used in the present thesis because it enables a thorough examination of high-frequency variability in the X-ray light curve. Especially the highest possible frequency of 4000 Hz allows us to easily see the variability at the inner radius where the accretion disk encounters the magnetosphere of the NS. An introduction of *RXTE* and a more detailed description of the data are given in section 4.1.

In its light curve, Bursting Pulsar shows quasi-periodic oscillations (QPOs) at frequencies both above and below the persistent pulsation (high- and low-frequency, respectively). Zhang *et al.* (1996) [21] found that the PDS in range from 15 to 100 Hz followed a power-law with an index  $-0.4$ , and QPOs appeared around frequencies 20, 40 and 60 Hz. For a truncation in the standard gas-pressure dominated disk, the Keplerian frequency of the inner radius should be proportional to  $L^{3/7}$  and the beat frequency  $\omega_{\text{beat}}$  between the Keplerian frequency at the inner radius  $\Omega_{\text{K}}(r_{\text{in}})$  and the spin frequency  $\Omega_*$  of the NS should be  $\omega_{\text{beat}} = \Omega_{\text{K}}(r_{\text{in}}) - \Omega_*$  [22]. Zhang *et al.* (1996) claim that the QPOs cannot be the beat frequency since taking  $\omega_{\text{beat}} = 2\pi f_{\text{QPO}}$  for GRO J1744–28 yields the expected relation  $f_{\text{QPO}} = f_{\text{in}} - f_* \approx f_{\text{in}} \propto L^{3/7}$  for corresponding frequencies, which is not

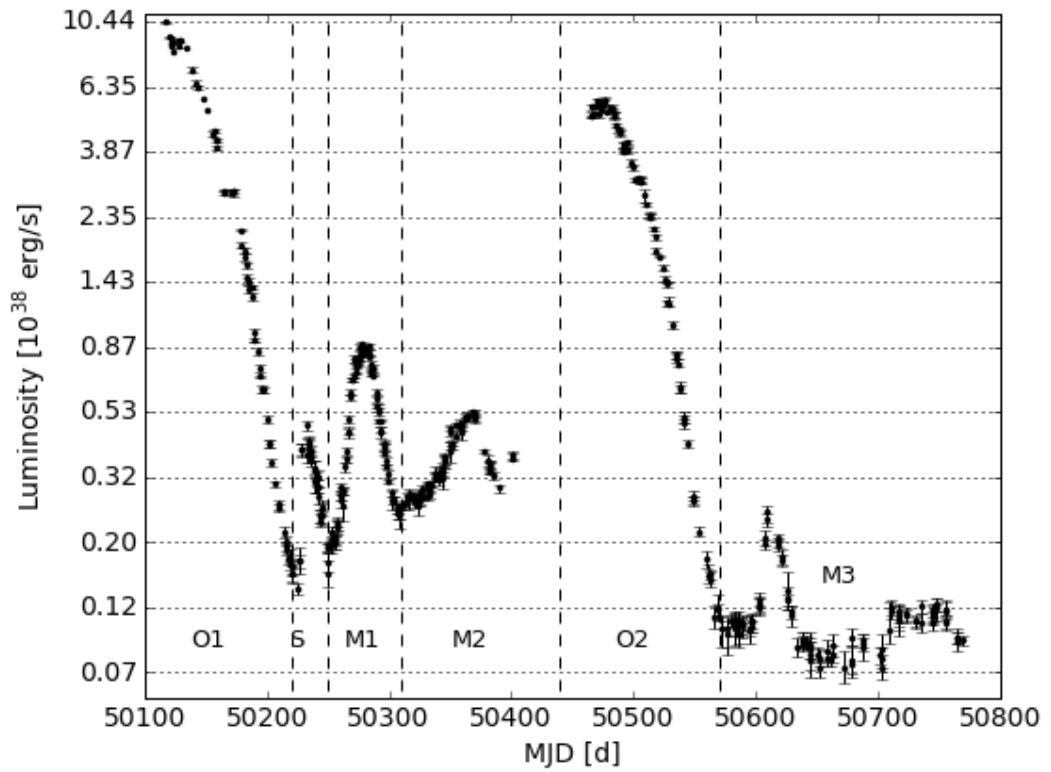


Figure 2. Long-term X-ray light curve with luminosities given in 2.5 – 45 keV band. Luminosity bins, in which PDS were averaged together, are shown with horizontal dotted lines. The light curve has been divided into separate time periods with vertical dashed lines: O1 and O2 mark the 1st and 2nd outburst, S marks the period when the spectrum showed a soft excess and M1, M2 and M3 are the low-luminosity periods with mini-outbursts.

attested. Below the frequency of regular pulsations, there were QPOs seen at 0.4 Hz in spectrally hard post-burst shoulders that occurred after about one tenth of bursts [23].

The energy spectrum of the source can be approximated with an absorbed power-law with index  $\Gamma \approx 1.3$  and an exponential cutoff at  $E_{\text{cut}} \approx 20$  [17]. Hydrogen column density was measured from spectra to be around  $5 \times 10^{22}$  H/cm<sup>2</sup> towards the Galactic Center, in which the source is assumed to be located at a distance of around 8 kpc [24, 25].

Recently, a cyclotron absorption line at 4.7 keV was found in the spectrum extracted from *XMM-Newton* instrument EPIC/pn data, indicating a surface dipole magnetic field strength  $B \approx 5 \times 10^{11}$  G [5]. Doroshenko *et al.* (2015) [7] reported an independent finding of an absorption-like feature at 4.5 keV from *BeppoSAX* data. This value for  $B$  is in agreement with an earlier upper limit of  $6 \times 10^{11}$  G, above which the source would be in propeller regime, that is, the accretion would be inhibited as the angular velocity of the accretion disk matter at the inner disk edge would be slower than the neutron star spin frequency [15]. Entering the propeller regime below  $L \approx 2 \times 10^{37}$  erg/s in 2 – 60 keV band was suggested to account for reduced pulse fraction during the time period from MJD 50210 to 50260, giving  $B \approx 2 \times 10^{11}$  G [26]. Also, Stark *et al.* (1998) [18] reported that the period derivative was negative at the same time period, but used a value of  $7 \times 10^{35}$  erg/s for luminosity in 2 – 60 keV band. Rappaport & Joss (1997) [27] examined the evolutionary history models, and assuming an equilibrium state (magnetospheric border at the corotation radius) derived a range  $(2 - 7) \times 10^{11}$  G, with  $2.7 \times 10^{11}$  G being the most probable. However, Degenaar *et al.* (2014) [28] derived a range  $(2 - 6) \times 10^{10}$  G using the inner radius  $\sim 2 \times 10^7$  cm, which they got from the model DISKLINE used in XSPEC for fitting the broad iron emission feature as reflection from the innermost disk.

The start of a new outburst was observed on 13 February 2017 [29]. Russell *et al.* (2017) [30] report that the X-ray luminosity in 2 – 10 keV was  $1 \times 10^{36}$  erg/s. The source is followed with great anticipation of what the current outburst will reveal about the accretion dynamics in this complex system. Meanwhile, we can analyse already existing data.

### 3 Disk-magnetosphere interaction

#### 3.1 Accretion disk

In Roche lobe overflow, which is also thought to take place in GRO J1744–28, matter flowing from the companion initially has angular momentum with respect to the primary. When matter falls towards the compact object, it follows a trajectory leading into a formation of a Keplerian ring of matter at the circularization radius. Matter around the central object is in differential rotation with Keplerian frequency  $\nu_{\text{K}}(R)$  given by equation

$$2\pi\nu_{\text{K}} = \sqrt{\frac{GM}{R^3}}, \quad (2)$$

where  $R$  is the radius of the orbit given by the distance from the central object. In order for the matter to be accreted onto the NS from the circularization radius, it needs to get rid of its angular momentum through mechanisms connected to disk magnetic fields and turbulence. Taking into account the differential rotation and inner forces of the plasma, hydrodynamical viscous diffusion is able to spread the initial ring of matter into a disk [31]. In the diffusion process, angular momentum is transported outwards by decreasing amounts of receding matter while rest of the matter is accreted onto the central object.

To account for the lack of an exact description of angular momentum transport mechanisms, Shakura & Sunyaev (1973) [11] adopted an  $\alpha$  prescription for linking tangential stresses to density and sound speed. Such disks are called standard or  $\alpha$  disks and for turbulent mechanisms  $\alpha < 1$  and can be a function of radius. In the present thesis,  $\alpha$  is assumed to be 0.1. Modern theoretical considerations have shown that disk viscosity can be explained by magnetorotational instability (MRI) [32]. In MRI, turbulence is created when weak, frozen-in magnetic fields try to keep the rotation rigid. Two mass elements are magnetically tied to one another so the outer mass element is accelerated on its orbit by the drag of the inner element. This drives the outer element further away from the NS while the inner element is slowed down and falls towards the NS. This drives the instability further until some stochastic reconnection relaxes the magnetic stresses.

When the matter spirals in towards the NS, part of the potential energy goes into the rotational kinetic energy, while another part goes to heat through the viscous processes. This heat will then be radiated from the disk surface. The remaining potential and kinetic energy will be released close to the NS surface. For a release of potential energy, the complete accretion luminosity  $L$  is given by  $L = GM\dot{M}/R$ , where  $\dot{M}$  is the mass accretion rate. Since flux  $F = L/(4\pi D^2)$ , where  $D$  is the distance, the observed flux is also related to the mass accretion rate, although possible beaming and anisotropy mean that the correspondance is not always one-to-one. Uncertainties in the estimate for the distance also affect the luminosities. The radiation pressure from the central object will increase with mass accretion rate and ultimately the force exerted by the radiation on the accreting matter will balance the gravitational pull of the central object. For spherical accretion, this limiting isotropic luminosity is called the Eddington luminosity

$$L_{\text{Edd}} = \frac{4\pi GMm_{\text{H}}c}{\sigma_{\text{T}}(1+X)} \approx 1.4 \times 10^{38} \frac{M}{M_{\odot}} \text{erg s}^{-1}, \quad (3)$$

where  $m_{\text{H}}$  is the hydrogen mass,  $X$  its mass fraction and  $\sigma_{\text{T}}$  is the Thomson scattering cross section. In a NS, the magnetic field guides the accretion flow close to the NS and the formation of an accretion column allows for an anisotropic radiation field and super-Eddington luminosities [33, 34]. Such has to be the case in GRO J1744–28 with highly super-Eddington luminosities.

The component of gravitational force that is normal to the disk plane is balanced by a vertical pressure gradient. The pressure has contributions from gas, radiation, turbulent and magnetic pressures, but mainly gas and radiation pressure play a role. The dominating conditions in the disk change due to the heat released when approaching the NS, and the disk can be divided into three regions or zones. The outermost region, zone C, is gas pressure dominated (GPD) and the interaction between radiation and matter, opacity, is determined by free-free and bound-free absorption and other processes. In the middle region, zone B, the gas pressure still dominates over the radiation pressure, but the opacity is determined by scatterings from free electrons. The innermost region, zone A, is RPD

and opacity is provided by electron scattering. In these zones, other physical quantities of the disk, such as surface density and temperature, have different dependencies on the radius and mass accretion rate, and also the emission profiles are different. [11]

GPD disks are relatively thin, but the situation changes when radiation pressure becomes dominant. The relative disk thickness ( $H/R$ ) will increase in zone A and become almost independent of radius, but details depend on whether one assumes the disk to be optically thick or thin. Vertical structure of an  $\alpha$  disk was examined numerically by, e.g. Suleimanov *et al.* (2007) [35]. Chashkina *et al.* (2017) [36] have studied super-Eddington accretion and in their models the resulting RPD inner disk also have a high relative disk thickness. For strongly super-Eddington luminosities, the accreted matter may even form an optically thick accretion envelope over the entire magnetosphere [37]. Knowing the disk thickness is important because it affects for example the disk viscosity and through that the power spectra. The interaction between the disk and the magnetosphere at the inner radius, on the other hand, is directly reflected in the accretion column shape and in the resulting emission [34].

For the aforementioned reasons, it is very useful to estimate how large the zones are and where the magnetospheric truncation takes place. The transition from zone C to B is estimated by equating the different dominating opacities:

$$R_{BC} = 5 \times 10^7 m^{1/3} \dot{M}_{17}^{2/3} \text{ cm}, \quad (4)$$

where  $\dot{M}_{17}$  is the mass accretion rate in units of  $10^{17}$  g/s, solar chemical composition is assumed and the opacities are taken to have their characteristic values in the disk [35]. The border between zones B and A on the other hand results from a balance between gas and radiation pressures in the disk:

$$R_{AB} = 10^7 m^{1/3} \dot{M}_{17}^{16/21} \alpha^{2/21} \text{ cm}, \quad (5)$$

with similar approximations as in equation (4). In short timescales, these border radii can be approximated to change only with mass accretion rate. Locations of these borders at

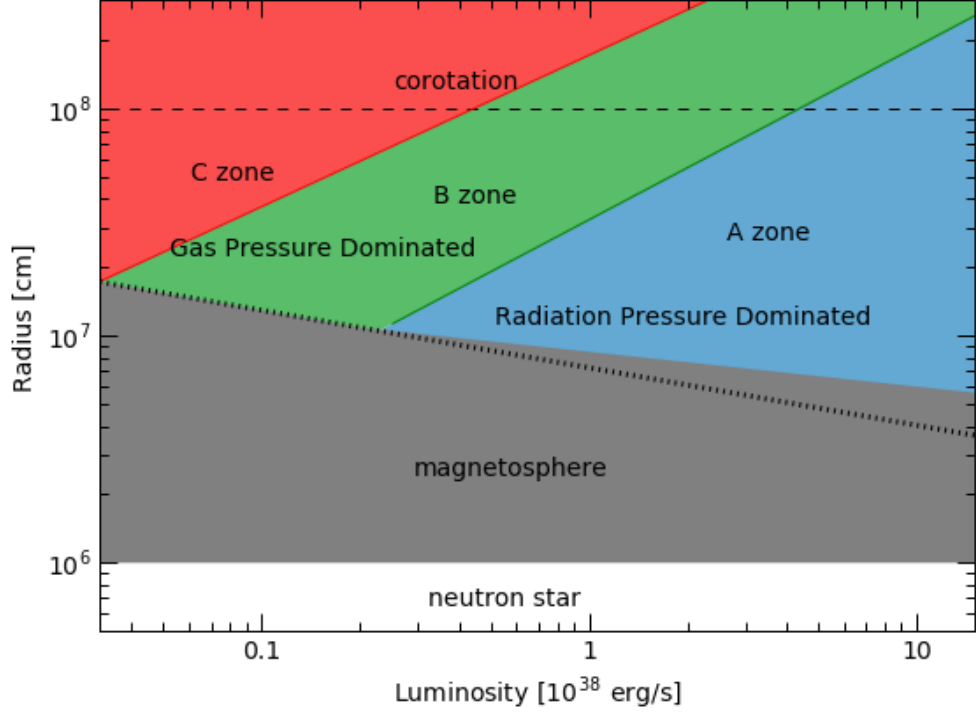


Figure 3. Slices of the accretion disk in radial direction at different accretion luminosities. Different zones are named and the corotation radius is shown with a dashed line for GRO J1744–28. The magnetospheric truncation radii for GRO J1744–28 are estimated from observations and the model of Ghosh & Lamb (1992) [38] with  $B \approx 3 \times 10^9$  G. In the model, the dependency of the inner radius on the luminosity changes when the truncation takes place in the RPD region instead of the GPD region, which is highlighted by the dotted line, showing the inner radius for a GPD disk. Determination of inner radii from the PDS of GRO J1744–28 is discussed in section 5.3.

different luminosities are shown in Figure 3 and the magnetospheric truncation radii are estimated for Bursting Pulsar from observations and Ghosh & Lamb (1992) [38] model. We see that already above  $L \sim 2 \times 10^{37}$  erg/s the inner disk becomes RPD and the magnetospheric truncation should take place in the zone A.

### 3.2 Magnetospheric truncation

The dipole component of the magnetic field reduces with distance as  $B \propto R^{-3}$ . This means that as the accretion disk extends towards the NS, it starts to experience stronger and stronger magnetic field of the NS. This will affect the accretion flow and the basic model of interaction is as follows: Far away, the disk flow is unperturbed by the magnetic

field and remains Keplerian. At some radius, where depending on the model either the magnetic pressure, energy density or stresses start to dominate, the disk flow is intercepted. This radius is called the magnetospheric radius (or inner/truncation radius). There is a boundary layer at the magnetospheric radius, where magnetohydrodynamical (MHD) instabilities start to transfer the matter from the disk into the magnetosphere, decelerating it to match the NS spin frequency. If disk matter at the inner radius has lower angular velocity than the stellar field, accretion may be inhibited by the propeller effect [39, 40]. Review of some properties of accretion disks around magnetized stars is provided in [2].

A simple way to estimate the magnetospheric radius is to set the magnetic pressure equal to the ram pressure of matter in spherical accretion. The resulting radius is known as the Alfvén radius

$$R_A = \left( \frac{\mu^4}{GM\dot{M}^2} \right)^{1/7}. \quad (6)$$

If we take this as the inner radius of an accretion disk, we see that when the mass accretion rate increases, the disk is able to push itself further into the magnetosphere, and the inner radius decreases. This simple consideration is not enough, because in accretion disks the matter has angular momentum as well. As discussed in Lamb *et al.* (1973) [41] and King *et al.* (2002) [4], the expression for the magnetospheric radius becomes

$$R_m = \xi R_A = 2.6 \times 10^8 \xi m^{1/7} R_6^{10/7} B_{12}^{4/7} L_{37}^{-2/7} \text{ cm}, \quad (7)$$

where  $\xi$  is a parameter describing the geometry of the accretion flow,  $R_6$  is the radius of the NS in units of  $10^6$  cm and  $L_{37}$  is the luminosity in  $10^{37}$  erg/s. Here, the critical feature is the ratio of magnetospheric radius to Alfvén radius,  $\xi$ , which is typically taken to be  $0.5 - 1$ , as was calculated by Ghosh & Lamb (1979) [42] and later studied both theoretically and numerically [2]. When determining the magnetic field strength from the inner radius using equation (7), one should take into account the uncertainties in  $\xi$ . For example, Chashkina *et al.* (2017) [36] proposed a new model for the RPD inner disk and they find that  $\xi$  can vary in such a way that the inner radius becomes independent of the mass accretion rate.

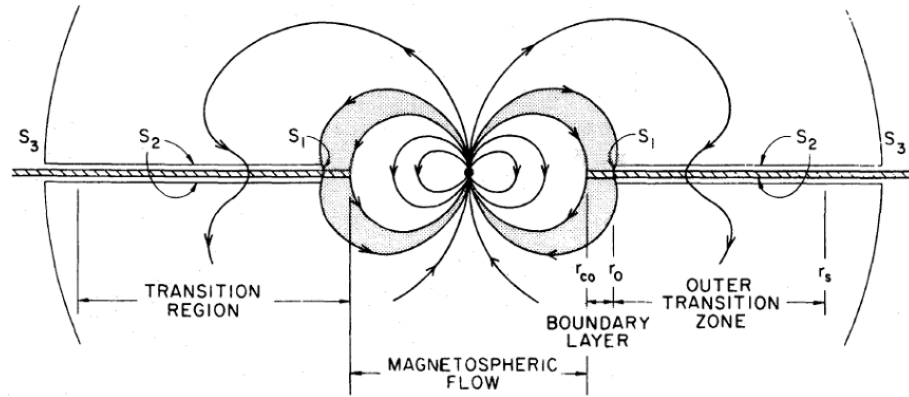


Figure 4. Ghosh & Lamb (1979) [42] model for the magnetospheric truncation. The disk starts to interact with the magnetosphere in the outer transition region, where the velocities are still Keplerian. Closer to the NS, a narrow boundary layer forms, where the magnetic field starts to slow down the disk matter, until it's completely bound to the field. Then at the truncation radius, the matter will flow from the disk plane along magnetic field lines onto the magnetic poles.

In the model developed by Ghosh & Lamb (1977-1979) [43], the interaction with a thin GPD disk takes place in a transition region with a wide outer region and a narrow inner region. Outside the transition region, the magnetic fields are screened by currents in the outer transition region, which has a slow radial drift but Keplerian angular velocity. Closer to the Alfvén surface, the magnetic field starts to invade and thread the disk due to Kelvin-Helmholtz instability, turbulent diffusion and magnetic field reconnection. This leads to the formation of a narrow boundary region where the angular velocity of the disk matter is reduced (in case of accretion) to match the angular velocity of the NS magnetosphere. The inner radius of this zone is determined by the equality between magnetic field stresses and material stresses. Their model assumes that the magnetic field lines are not twisted. Figure 4 shows a disk-magnetosphere cross-section as described in the model. The model of Ghosh & Lamb, however, has been criticized for having an unphysically high magnetic diffusivity in the disk [44].

What if the disk is not entirely GPD? As discussed in section 3.1, at high luminosities, the inner disk is expected to become RPD even when the disk is truncated. The threshold luminosity for zone A to appear can be estimated from the condition that the standard

inner radius  $R_m$  given by equation (7) and the limiting radius between disk zones A and B  $R_{AB}$  given by equation (5) become equal:

$$L_{A,38} > 3.4\xi^{21/22} B_{12}^{6/11} m^{6/11}. \quad (8)$$

For example, in the case of GRO J1744–28, the threshold is  $L_A > 6 \times 10^{37}$  erg/s for  $B = 10^{11}$  G. Much higher luminosities are reached in both of the examined outbursts (see Figure 2) and we definitely should have a RPD inner disk. This can affect the truncation process in many ways, e.g. changing the  $\xi$  in equation (7).

Physical conditions are indeed different in different disk zones, and where magnetospheric truncation happens, it affects how the truncation radius depends on the system parameters. Therefore it is better to write the inner radius in a general form

$$R_{\text{in}} \propto \dot{M}^a \mu^b M^c, \quad (9)$$

where exponents  $a$ ,  $b$  and  $c$  depend on the zone where truncation takes place and boundary layer description [38]. Exponents for GPD and RPD one-temperature, optically thick disk models are given in Table 1 [38]. Truncation in RPD region was examined by White & Stella (1988) [45], but Ghosh & Lamb (1992) [38] claim that the results for the inner radius in this paper are wrong since White & Stella considered the height of an unperturbed disk instead of the height of the boundary region. Observing how the inner radius depends on the mass accretion rate may then reveal which of the models works at a given luminosity and also whether the inner disk is RPD or GPD at a given luminosity. A schematic of the disk in different luminosities is shown in Figure 3 where the inner radius is based on observations of GRO J1744–28 and on the Ghosh & Lamb (1992) [38] model where the dependency of the inner radius on luminosity changes when a RPD inner region forms. The conditions in the inner disk also affect the angular momentum transport between the disk and the magnetosphere.

At some radius from the NS, the Keplerian angular velocity in the disk is equal to the NS rotational velocity  $\Omega_*$ , and this radius is called the corotation radius  $R_{\text{co}} =$

Table 1. The dependency of the inner radius on the physical parameters<sup>1</sup>

Disk model	$R_{\text{in}} \propto \dot{M}^a \mu^b M^c$		
	Value of $a$	Value of $b$	Value of $c$
Gas pressure dominated (GPD)	−0.25	0.58	−0.21
Radiation pressure dominated (RPD)	−0.15	0.51	−0.13

<sup>1</sup> After Ghosh and Lamb (1992) [38].

$(GM/\Omega_*^2)^{1/3}$ . In the standard model, if the inner radius of the accretion disk is located inside the corotation radius, the magnetosphere can transfer angular momentum from the disk onto the NS. Depending on the model for the magnetospheric truncation, this picture can change, especially if winds carry angular momentum away, or if magnetic links to the disk outside the corotation radius are being established [46]. If the truncation radius is outside the corotation radius, the source is thought to enter a propeller regime, as the speed of the magnetosphere will exceed the speed of the matter in the disk and shocks will inhibit accretion [39, 40]. Angular momentum will be deposited into the disk and may warm the disk substantially [47]. Sources with an inner radius close to the corotation radius are said to be accreting in equilibrium.

For pulsars, such as GRO J1744–28, accretion torques can be calculated from observations of the derivative of NS spin period (or frequency). The standard dependency for the inner radius given by equation (7) in a GPD regime results in frequency derivative  $\dot{f} \propto L^{6/7}$ . This was not observed for GRO J1744–28, but instead, a larger exponent was found with  $\dot{f} \propto L^{0.96}$  [48]. Similar spin-up was discovered by Sanna *et al.* (2017) [49],  $\dot{f} \propto L^{0.93}$ . As they note, such a higher value of the exponent is as expected in Ghosh & Lamb (1992) model for an RPD disk,  $\dot{f} \propto L^{0.92}$ . A torque model by Kluźniak & Rappaport (2007) [47] also predicts a higher expected relation to  $L^{9/10}$  for a GPD disk and for a magnetic field with azimuthal component related to the poloidal component as  $B_\phi \simeq B_z(1 - \omega(R)/\Omega_*)$ . Thus by itself, this piece of evidence for GRO J1744–28 is not enough to determine, whether the disk is in a RPD state or whether the models of Ghosh

& Lamb are correct.

There are indeed many disk models. Some more recent considerations allow outflows from the disk, which greatly affect the angular momentum transport and spin-up of the accreting star. Shu *et al.* (1994) [50] considered young stars and thus smaller conductivities and shear of the innermost disk. Their magnetic field only penetrates the disk close to the strongly pinched magnetospheric boundary, which also allows the generation of a magneto-centrifugal wind. In the model of Lovelace *et al.* (1995) [51] magnetic field lines can twist, which leads to a region of open field lines and launching of magnetically driven outflows. Kluźniak & Rappaport (2007) [47] examined magnetically torqued thin accretion disks, which are linked to the magnetosphere over a wide range of radii, for two different models of azimuthal magnetic field. Matt & Pudritz (2005) [52] also considered young stars and find that differential rotation opens field lines and weakens the spin-down of NS due to significant torques of the wind.

In spite of all the differences in these models, the basic picture remains the same: the accretion disk is truncated in some disk zone and the inner disk radius depends on the system parameters, getting closer to the NS as the mass accretion rate increases. But what about Keplerianity of the disk? For most of the theoretical work, the disk remains Keplerian up to a narrow region where the matter is decelerated. The deviations from Keplerianity are  $\lesssim 10$  per cent for a GPD disk with possible outflows [47]. White & Stella (1988) [45] mention that in a RPD inner disk, orbital velocities start to deviate from Keplerian only in a relatively narrow region of the innermost disk, where the radial velocities may increase as the matter is decelerated. Accretion disks around stars with inclined magnetic dipoles were simulated by Romanova *et al.* (2004) and they found that for low inclinations of the dipole (as expected in GRO J1744–28) the disk velocities remain close to the Keplerian velocities up to steep decrease at the magnetospheric border, causing a similar 10 per cent error in radius estimated from the maximal angular velocity. Chashkina *et al.* (2017) [36], on the other hand, find deviations of a few per cent from

Keplerianity for the RPD disk. Thus it is motivated to assume that disk is nearly Keplerian up to a narrow boundary region at the inner radius.

What actually enables accretion via the magnetosphere and what happens after the matter leaves the disk? The matter flow in the disk plane is intercepted when the magnetic field is strong enough to bind the matter. Above the threshold of  $B \sim 10^9$  G, the cyclotron radius of an electron is reduced beyond the standard atomic radius and matter becomes confined in transverse direction with respect to magnetic field lines [53]. In the boundary region, magnetic dissipation will heat the disk so that the vertical pressure gradient will overcome the gravitational pull and push the matter along the magnetic field lines, that is, the only possible route [54]. Matter that is guided onto the magnetic poles of the NS will initially form an accretion mound. Rest of the potential and kinetic energy will be released there. If the mass accretion rate is high enough,  $L \gtrsim 10^{37}$  erg/s, radiation pressure will start to slow down the matter, which is falling onto the poles, already above the accretion mound and an accretion column will start to form [33]. The size and shape of the column depend on the distance of the accretion disk from the NS and the disk height at the inner radius, both of which vary as a function of mass accretion rate [34].

A complete, self-consistent model that would explain all the features, is nonetheless difficult to construct as various time-dependent parameters and stochastic processes shape the interaction. The magnetic field lines will most likely be deformed by disk matter, but details depend on the model. If the disk is taken to be diamagnetic, there are no components of the NS magnetic field inside the disk (the vertical component disappears on the disk surface), but this picture may be unrealistic. If diamagnetism is assumed, the closed field lines of the magnetosphere are ‘pinched’ by the surrounding disk ring, and the magnetic pressure on both sides of the disk and in the pinched field will increase and possibly even prevent accretion. In a more realistic picture, the field may connect to the disk, penetrate it or thread the disk in a stochastic way, which should happen at least at the boundary layer to allow accretion, and opening of the field lines can give birth to winds.

If the axis of the magnetic field is not aligned with the rotational axis, the shape of the magnetospheric border is also affected. Since the strength of a dipole field is weaker at equator, the disk periodically encounters stronger and weaker magnetic fields. The cut of the magnetosphere in the disk plane is not a circle but an oval shape, so the fronts can cause shocks in the disk matter [39, 46]. The disk may also be warped due to the different magnetic pressures above and below the disk plane [55]. Warping, on the other hand, will affect how much of the radiation coming from the NS is intercepted by the disk and produce further pressure on the disk. These are just a few of the possible ways of interaction. The only way to find out what actually happens in real objects is a comparison to model predictions and observations. The variability of flux at different timescales, in particular, serves as a tool for probing the complex interaction between an accretion disk and a magnetosphere.

### **3.3 Accretion disk as the source of variability in flux**

Random flux fluctuations over a wide range of timescales, also known as flicker noise, are an ubiquitous feature in light curves of X-ray sources. Although disk flaring and coronal reconnections have been invoked as explanations for black hole systems, these models fail to explain the similar behaviour witnessed in NSs, where most of the emission is released close to the NS surface. Variability timescales which are longer than the characteristic timescales at the NS surface must be due to fluctuations in the local mass accretion rate. These fluctuations arise in the accretion disk, where MHD turbulence creates stochastic variability on different timescales at different radii [32]. The propagation of these fluctuations along the disk flow and the resulting PDS can be described by the perturbation propagation model [6].

Initial fluctuations in mass accretion rate are related to the MHD processes which have Keplerian timescales (see equation (2)) [56]. As discussed in section 3.1, the disk matter is spread by viscous diffusion, and the radial drift inwards enables the propagation of

fluctuations. The propagated perturbations originating in outer disk radii are superposed with new fluctuations created at smaller radii. The fluctuations are also damped strongly, if their frequencies are higher than local viscous frequencies  $f_v(R) = 1/t_v(R)$ , where  $t_v$  is the local viscous timescale at radius  $R$ .

PDS is a powerful tool for examining the variability in the light curve, which arises from the process of superposition and damping of perturbations. For a standard disk, the resulting power has a power-law shape with an index from  $-1$  to  $-1.5$  over a range of frequencies. If one takes into account the outer and inner radii, the power law becomes doubly broken. The low-frequency break corresponds to the viscous frequency of the outer disk radius because mass accretion rate variability is not suppressed below that frequency. The high-frequency break, on the other hand, corresponds to the Keplerian frequency of the inner disk since the accretion disk does not produce variability above this frequency. These models also predict the root mean square (rms) variability in power to be linearly proportional to the flux. [6, 57, 58, 59]

The break in power has been observed in several X-ray pulsars that are accreting in equilibrium [60]. The break in these sources can be explained by the transition from accretion via the disk to accretion via the magnetosphere at disk corotation radius (equals truncation radius). In these sources the break is close to the NS spin frequency as expected. This provides evidence for the picture that the orbital velocities at the inner disk radius correspond to the Keplerian velocities (excluding the narrow transition region). Thus we can assume this to hold also in sources that are not in equilibrium.

The inner radius, however, does not remain the same. A higher mass accretion rate leads to an increase of gas pressure in disk and enables the disk matter to push the inner disk further into the magnetosphere. An increase in the accretion rate means that the total luminosity should increase as well. As the break in power at the break frequency corresponds to the Keplerian frequency at the inner disk radius, the break frequency is expected to move to higher frequencies when the luminosity increases (and vice versa).

Table 2. The dependency of the break frequency on the physical parameters<sup>1</sup>

Disk model	$f_b \simeq \nu_{K,0}(L/L_{\text{Edd}})^\alpha \mu_{27}^\beta m^\gamma$			
	$\nu_{K,0}$	Value of $\alpha$	Value of $\beta$	Value of $\gamma$
Gas pressure dominated (GPD)	430	0.38	-0.87	0.82
Radiation pressure dominated (RPD)	210	0.23	-0.77	0.703

<sup>1</sup> After Psaltis and Chakrabarty (1999) [61] based on Ghosh and Lamb (1992) [38].

Combining the equations for Keplerian frequency given by equation (2) and the standard magnetospheric radius for GPD inner disk given by equation (7) results in

$$f_b \propto \dot{M}^{3/7} \mu^{-6/7} M^{10/14}. \quad (10)$$

This standard  $f_b \propto L^{3/7}$  is seen in, e.g. pulsar A0535+26 [60]. If the inner disk is not a standard GPD disk, as expected for GRO J1744–28, this picture may change. In general, we can transform the formula for the inner radius given by equation (9) into corresponding break frequencies as

$$f_b \simeq \nu_{K,0} \left( \frac{L}{L_{\text{Edd}}} \right)^\alpha \mu_{27}^\beta m^\gamma, \quad (11)$$

for which the scaling constant  $\nu_{K,0}$  and exponents  $\alpha$ ,  $\beta$  and  $\gamma$  are given for GPD and RPD models in Table 2, as was examined by Psaltis & Chakrabarty (1999) [61] based on Ghosh & Lamb (1992) [38] (compare to the exponents given in Table 1). From observations we can determine how the break frequency depends on the luminosity and thus infer the conditions in the inner disk.

But can the variability really be assumed to come only from the disk itself? For a possible accretion envelope, the timescales are much shorter or in the case of precession, much longer. Photon bubble oscillations in the accretion column have been suggested to account for some of the noise in a range from 10 to  $10^4$  Hz, especially when the magnetic field is weaker than  $2 \times 10^{13}$  G [33]. These were used to explain the QPOs seen in GRO J1744–28, but the model could not explain the dependency of the centroid frequency on the luminosity [21]. In almost all of the cases, photon-bubbles are not seen

even if expected [62]. So even if there was some noise coming from other sources than the disk, the most dominant source that produces noise in range from hertz to kilohertz scales seems to be the disk.

Various other types of QPOs are also observed in PDS of accreting X-ray sources. Two peaks of QPOs in the kHz range with constant separation are seen in many sources [63]. These have been explained by the beat-frequency model, where the oscillations arise from both the inner radius and also from beating between the orbital frequency of the inner radius and the stellar frequency [22]. Some QPOs may come from the precession of the magnetically bent disk [2]. Photon bubble oscillations have been proposed as an explanation for some of the QPOs but the model predictions do not match the observations and often the QPOs are not observed even if expected [64, 62]. Resonant shear Alfvén waves in the magnetosphere may be an explanation to QPOs [65]. Flaring resulting from magnetic reconnection between the disk and magnetosphere may also cause some quasi-periodic activity [46].

### 3.4 Instabilities and type II bursts

Instabilities work to bring the system closer to an equilibrium. Thermal and viscous instabilities make the RPD disk unstable [66]. At the magnetospheric boundary, instabilities allow matter to slip into the magnetosphere in the transition region: Kelvin-Helmholtz instability works on a two-fluid interface with velocity shear between the adjacent layers, and it causes turbulent mixing. Rayleigh-Taylor instability occurs if a denser fluid is positioned over a lighter fluid in a force field. Magnetic reconnection is a change in field line structure towards a more stable configuration, reducing magnetic stresses. Magnetic dynamo action in the accretion disk may also initiate large flares as noticed in simulations by King *et al.* (2004) [56]. These rarely occurring flares in flux might be a cause for isolated type II bursts seen in some sources, such as SMC X-1 (see [67]).

There are two types of X-ray bursts: type I and type II. Type I bursts result from uns-

table thermonuclear burning of matter which has accreted onto the NS surface. They are common in NSs in LMXBs, but are not seen in pulsars with strong magnetic fields as in those objects, thermonuclear burning is stable. Type I bursts are characterized by sudden rises and long, exponential decays with spectral softening caused by an additional thermal component. Type II bursts on the other hand are seen only in some sources, most notably Bursting Pulsar and Rapid Burster. During a short period of enhanced mass accretion rate, there is more potential energy of accreting matter to be released. This short-lived enhancement in mass accretion rate arises from some sort of instability in the accretion disk and the bursts are characterized by quick rises and decays. Dips in total source flux are also associated with the bursts, and they are thought to be caused by a depletion of some mass reservoir in the disk. For GRO J1744–28, this can be seen in Figures 6 (A) and (B).

Only type II bursts are seen from Bursting Pulsar [14, 15]. Complete lack of type I bursts may be explained by the very high mass accretion rate [68, 69, 48]. Some type I bursts were seen at lower luminosities, but they were identified to be from other sources in the same field. Similar type II bursts have been observed in Rapid Burster (MXB 1730–2335), but Rapid Burster also shows type I bursts. The bursts from GRO J1744–28, however, are not explained by the traditional relaxation oscillator model, since there is no clear correlation with the burst fluence and time to the next burst [14]. During the bursts, the dead time may have a large effect on the observed count rates. It was, however, shown that even in a wide range of luminosities (and count rates) the ratio of the burst fluence to the persistent flux remains almost a constant when the dead time is taken into account [70].

There is also another similarity between Rapid Burster and Bursting Pulsar, low-frequency postburst QPOs [23]. Despite this, it has been discussed that none of the models which could explain the type II bursts of Rapid Burster agree with the observations of Bursting Pulsar [15]. The current consensus still is that some mechanism in the boundary region between disk and magnetosphere should still play a role in the initiation of bursts.

Cannizzo (1996) [19] examined the Lightman-Eardley instability [20] of an accretion disk in time-dependent simulations based on various previous works [71, 72]. He noted that in earlier work, the viscosity parameter  $\alpha$  had been set to equal its maximal value of 1 and that the inner disk edge was set very close to the central object so that the resulting bursting interval was too short for GRO J1744–28. Changing these to values closer to realistic estimates, produced bursts and light curves, shown in Figure 5. The  $\sim 10^3$  s recurrence times, 10 s bursts and post-burst dips all qualitatively match those of Bursting Pulsar, as seen in Figure 6 A. Cannizzo showed that the Lightman-Eardley instability stays in linear regime due to enhanced mass loss rate from the inner edge of the accretion disk. A cavity forms in the inner disk due to the loss of matter in bursts and part of the accreted mass goes into replenishing this, instead of being accreted onto the NS surface. The light curve then shows a dip and a recovery period.

Further honing the model in 1997 [73], Cannizzo could also explain pre-burst fluctuations seen in flux around a certain luminosity,  $L \approx 3 \times 10^{38}$  erg/s. This corresponds to his calculation of the critical mass accretion rate above which the inner disk starts to become RPD. The fluctuations result from oscillations of local heating and cooling rates with increasing amplitudes. These cause oscillations in the ratio of radiation pressure to the total pressure and when the ratio exceeds some threshold, the disk instability leads to bursts. Above this critical mass accretion rate, the bursts do not show pre-burst oscillations, as is the case in most of the bursts from GRO J1744–28 during outburst peak. The model, however, cannot explain why type II bursts are not observed in other accreting NSs with similar parameters. Results are given in section 5.1.

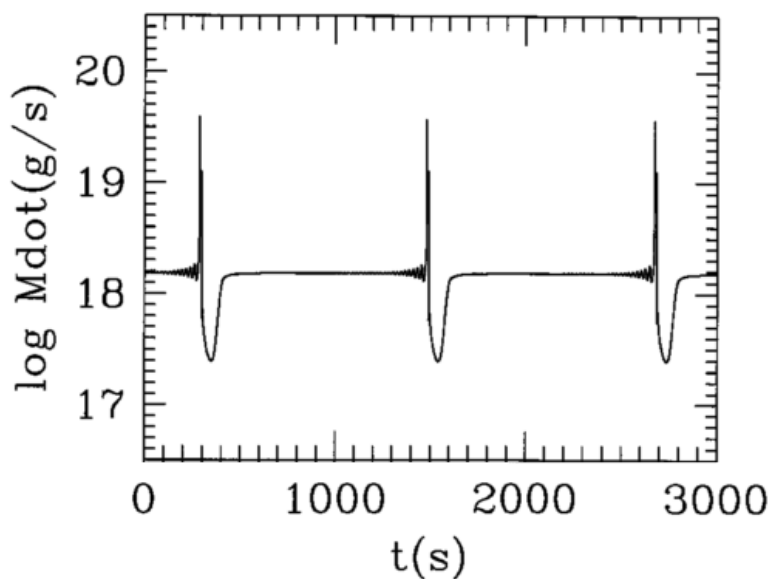


Figure 5. Type II burst light curves seen in a 3000 s run of Cannizzo’s model with a background mass accretion rate of  $\dot{M} = 1.5 \times 10^{18}$  g/s into the outer disk [19].

## 4 Methods

### 4.1 Data reduction

#### 4.1.1 Rossi X-ray Timing Explorer

Nasa’s high-time-resolution satellite mission, Rossi X-ray Timing Explorer (*RXTE*) was launched on December 30, 1995 into a low-Earth orbit and was decommissioned in January 2012. It had two main experiments on board, a large-area proportional counter array (PCA), with a total effective area of  $\sim 0.7$  m<sup>2</sup>, and a high-energy X-ray timing experiment (HEXTE). Both of them had a field of view of 1°. The satellite also contained an all-sky monitor (ASM) for surveying the sky. The *RXTE* data is publicly available in HEASARC archives.

For the present thesis, the PCA data were used. The non-imaging instrument consisted of 5 independent proportional counter units (PCU) operating in 2 – 60 keV energy range. The working principle of a proportional counter is the ionization of gas particles by X-ray photons in the detecting volume, where the ions are then accelerated onto the anodes. The

detection signal depends on the energy of the ionizing particle with some proportionality. In a PCU the incoming X-rays are collimated into the main detecting volume which is filled with a mixture of Xenon (90 per cent) and Methane. There were three detecting layers with anode wire grids. Non-X-ray background events were discriminated with the Propane-filled front anticoincident layer. [74]

Experiment Data System (EDS) formed the actual data files with different modes (e.g. Binned and Event) from the events observed. Using the EDS with four event analysers, a time resolution of  $1 \mu\text{s}$  and a spectrum with up to 256 energy bins in 2-60 keV range could be reached for PCA data [75]. The type of data files is flexible image transport system (FITS) with the data given in a table form and additional information in headers.

#### 4.1.2 Timing analysis

Extraction of light curves and spectra from data files can be done with tools from Heasoft software package v. 6.19 [76] and following the RXTE Cook Book guide. From each observation the data configuration with the best time resolution was chosen. For the first outburst this was almost entirely single-bit mode in science array format, using two energy bands (approximately 1–10 keV and 10–100 keV) and time resolution of  $244 \mu\text{s}$ . The rest of the chosen files were mostly in science event format with  $122 \mu\text{s}$ -resolution, collected over the entire *RXTE/PCA* energy range.

A Perl code was constructed for handling the data extraction process: there is an initial filter file corresponding to each observation data file, and these filters show for example the pointing and if the satellite passed over the South Atlantic Anomaly (SAA) where the particles of Van Allen belt increase the radiation level and all the PCUs were turned off. Due to a discharge in PCU3 and PCU4, the units were now and then individually shut down for some time. This resulted in a different number of PCUs being on at a given time. That's why data only from PCU2 were used for this work, and the extraction choice was included using `MAKETIME` with filter files. For Event modes, a bitmask had to be created

with FSELECT to remove clock events from the data.

Light curve extraction was done with SAEXTRACT for Binned modes and with SEEXTRACT for Event modes using good time intervals (GTI) for the data. Following the standard procedure, good columns were taken, binsize was set to the maximal time resolution and the binning was done as rate (total accumulated counts / binsize). The light curves were then handled using Python code with the Anaconda package and its Astropy FITS file handling. Scipy and Numpy were the most used packages, providing means of analysis and data handling.

Figure 6 (A) depicts a part of a typical short-term light curve in the high luminosity state showing two burst cycles with quiescent, burst and depression phases. The bursts were fitted with an asymmetric Gaussian curve, which consists of two halves taken from two different Gaussian curves with the same center value and normalization but different widths. The burst time period was taken to be an interval of four standard deviations around the center value. Post-burst period was taken as the time after burst that it takes for the 10 s average of flux to return to within 5 per cent of the pre-burst level or to stabilize at a new flux level. The flux does not always rise to the pre-burst level so defining the post-burst periods was not always straight-forward.

The XRONOS package from Heasoft provided the timing analysis tools. The frequency of the regular pulsations was found with EFSEARCH. Then the tool EFOLD was used to get the pulse profiles, that is, the light curves folded over the pulse period. Pulse fractions were calculated as the ratio of maximal to minimal values of these folded light curves. The results are described in section 5.2. PDS were calculated using POWSPEC as described in section 4.2.

### 4.1.3 Spectral analysis

What *RXTE* observes, are photon counts so in order to get the total energy fluxes of the source, we must find out what were the energies of the counted photons, that is, the

energy spectrum. The spectrum for each observation was extracted from Standard-2 files by following standard guides provided by *RXTE* Guest Observer Facility. Standard-2 has a time resolution of 16 seconds and 129 energy channels in the spectrum. Spectra were extracted only from the persistent periods in light curves. The bursts and post-burst dips were left out, because the burst flux would be underestimated due to dead-time effects and sometimes the light curves had only partially captured the post-burst periods, during which the deficit in the mass accretion rate compensates the stored matter released in the burst. Standard dead time corrections were applied in the form of a multiplicative factor estimated using the Standard-1 data. Python codes utilizing PyXspec, an XSPEC adaptation, were constructed for spectral analysis.

The spectra between 2.5 and 45 keV were fitted with a model consisting of a photoelectrically absorbed power-law with an exponential cut-off, a blackbody curve and a Gaussian line profile (PHABS\*(POWERLAW\*HIGHECUT+GAUSS+BBODY)). The Gaussian line was added to account for the wide fluorescent iron  $K\alpha$  line, and its central energy was fixed to 6.7 keV and its width to 0.3 keV [7]. For these fits the blackbody temperature was fixed to 1.7 keV. The hydrogen column density was fixed to  $6.2 \times 10^{22} \text{ cm}^{-2}$ , the average value for all the observations.

According to the *RXTE* help desk, a systematic error of 1 per cent should be added in XSPEC when fitting *RXTE* data from bright sources [77]. However, even with this systematic error included, the values for reduced  $\chi^2$  remained too high. Hence the systematic error was increased to 2 per cent.

Figure 2 includes luminosities derived from the flux of energy interval 2.5 – 45 keV. The most prominent features should be mainly from Bursting Pulsar, except at the lowest luminosities when the background sources in the same field of view [18, 16, 26].

## 4.2 Power density spectra

Light curves of stellar objects show a great amount of variability with respect to time. A Fourier transform of a light curve, that is, a decomposition of the signal into sine waves with specific frequencies, gives a PDS. Since the data, a time series, is always of discrete nature and finite length, PDS have to be calculated on time intervals. Such a discrete Fourier transform can only reach frequencies in a band which is limited from below by the length of the time series,  $\nu_{\min} = 1/T$ , and from above by the Nyquist frequency,  $\nu_{\text{Ny}} = N/2T$ , which is half of the sampling frequency for  $N$  samples. The actual PDS is constructed by averaging together many discrete PDS to reduce the statistical noise and increase the signal.

Since observations are counting individual photons, there are fluctuations in the data following Poisson statistics. This leads to white noise with some non-zero mean and a variance about it, even if no periodic or secular variations are present. In Leahy normalization, the power will be normalized to the total number of photons, which will help in finding the statistical significance of variations. Then the level of Poisson noise will have a mean value of 2, but dead time and instrumental noise will affect this. [78, 12]

In my examination, the broadband PDS in 0.0625 – 2048 Hz range were normalized to the squared mean intensity according to the Miyamoto normalization in which integration of the PDS gives the amplitude of intensity variations with respect to the mean, that is, fractional rms variability. [79]

The program POWSPEC was used for calculating the PDS from the X-ray light curves. A list of light curves in a luminosity and time interval was given as input (see Figure 2 and the horizontal and vertical binning). The requirement for the same time resolution in listed data files meant that most of the observations made in the decay phase of the first outburst required special handling: first, files from two different energy bands (channel ranges 0 – 23 and 24 – 249) were rebinned and then added together to get the counts in the entire energy range of PCA. This caused some artefacts at the highest frequencies but

the PDS were already pure Poisson noise there so these parts could be left out.

When creating the high-frequency PDS in 1 – 4096 Hz range, the amount of Poisson noise in each PDS was estimated by averaging the nearly flat high-frequency part. The values were subtracted from the spectra, and the remaining spectra were multiplied by frequency. Some PDS from lower luminosity bins were excluded from the analysis due to poor statistics and possible background contamination. Resulting PDS are discussed in section 5.3.

## 5 Results and discussion

### 5.1 Bursts

Figure 6 (A) depicts a part of a typical short-term light curve in a high luminosity state showing bursts with quiescent, burst and depression phases. As noted already earlier, good qualitative match with the Cannizzo (1997) [73] model is observed. The depth of the post-burst dip became gradually lower and the transition from the burst to the dip became smoother as visible in Figure 6 (B). At the same time, burst shoulders (periods of higher flux level after a burst) had become longer in duration. The dips became undetectable in both outbursts at roughly the same luminosity,  $L \approx 1 \times 10^{38}$  erg/s.

In the first outburst, the bursts themselves disappeared approximately below the luminosity of  $5 \times 10^{37}$  erg/s, but the activity later resumed after the soft excess for some period of time with different burst profiles 6 (C) & (D). In the second outburst, bursting continued longer and disappeared only below luminosity  $2 \times 10^{37}$  erg/s, but this may have been due to inactivity of neighbouring X-ray sources. Similarly to the first outburst, there was a period of quiescence before some of the ‘rumbly’ behavior was attested again. The rumbly features might be explained by magnetic reconnection [46], and interestingly, light curves similar to the observed ones were produced in simulations of propeller regime with varying viscosity by Romanova *et al.* (2006) [80] (see figures 10 and 11 therein).

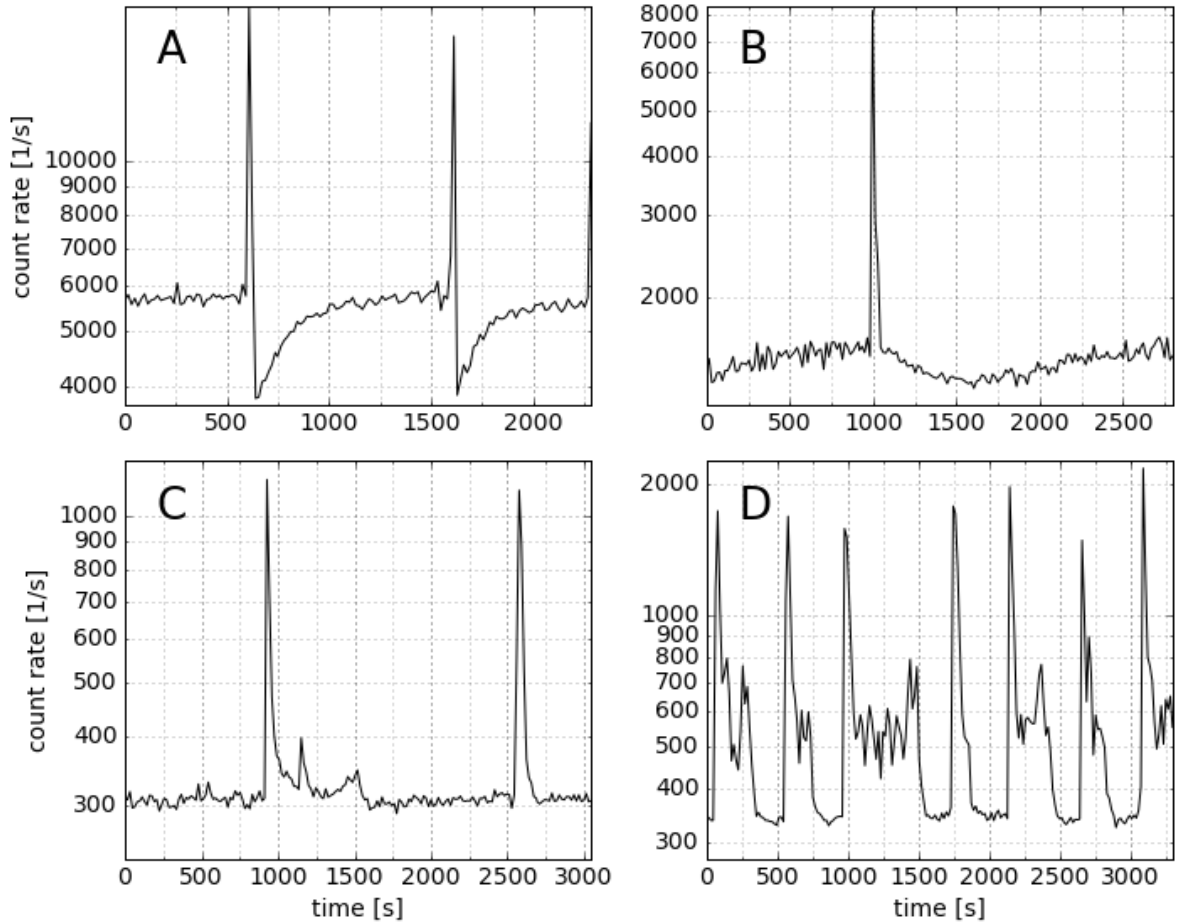


Figure 6. A compilation of light curves from different luminosities and times. Light curve (A) is a standard burst in high luminosity with post-burst periods marked. Light curve (B) shows a burst at  $L \approx 1 \times 10^{38}$  erg/s when the post-burst period had become much longer towards the end of outburst bursting activity. Light curve (C) with complex burst ‘shoulders’ is at a lower luminosity  $L \approx 3 \times 10^{37}$  erg/s, after the peak of the soft excess marked as S in Figure 2. Light curve (D) is at the end of the ‘rumbly’ stretch in the long-term light curve with high, regular shoulders after most of the bursts, and highly background-contaminated base level.

Threshold luminosity for the appearance of a RPD region in the inner disk was estimated to be  $L_A > 6 \times 10^{37}$  erg/s for  $B = 10^{11}$  G in section 3.2. We see a good match when we compare this to the luminosities, above which we see bursts. Thus Cannizzo's model that requires a RPD inner disk is a favoured explanation for the type II bursts.

## 5.2 Pulse profiles

In the outbursts, very sinusoidal pulse profiles were observed. During the decay phase of the first outburst, when the luminosity decreased from  $8 \times 10^{37}$  to  $3 \times 10^{37}$  erg/s, the pulse profiles were quite sinusoidal with some sloping either at the top or towards the bottom and the pulse fraction decreased from 10 to 6 per cent. In the decay phase of the first mini-outburst in the same apparent luminosity as in the major outburst decay, the pulse profile showed consistently an interpulse 'shoulder', and the pulse fraction stayed between 3 and 4 per cent. Since the pulse fraction was rather constant in the mini-outburst, the background sources could not be dominating over Bursting Pulsar and the mini-outburst indeed was caused by the source. During the soft excess, the pulse profiles were highly varying and the pulse fraction was only around 2 per cent. Examples of pulse profiles are shown in Figure 7.

Nishiuchi *et al.* (1999) [25] examined the pulse profiles at high luminosities and found that there is a large nonpulsed emission, which they hypothesized to be an indication of two-part accretion. The pulse fraction increases to higher energies. Taking the pulsed emission to come from the NS polar caps, they argue that the nonpulsed emission may then come from a larger emission region (e.g. entire NS surface). This may indicate that there are two accretion paths, both onto the magnetic poles and onto the surface due to a weak magnetic field or a multipole field configuration. One way to explain the low pulsed fractions is reflection. The emission from an accretion column is beamed towards the surface of the NS and then reflected [81, 82]. For a low inclination, as is expected for Bursting Pulsar, most of the observed pulsed emission would then be due to the reflected

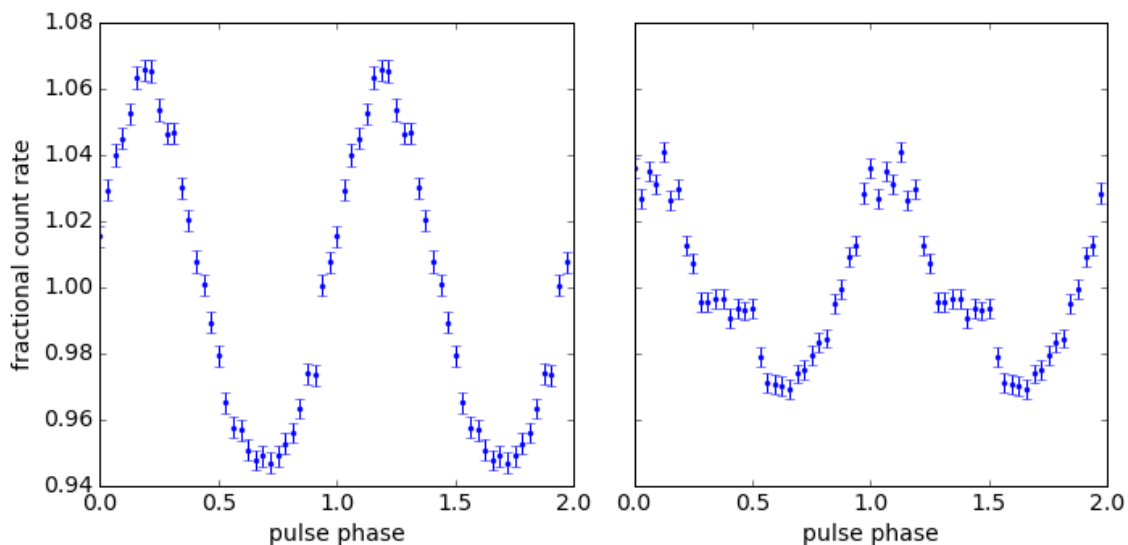


Figure 7. Pulse profiles for outburst decay phase and after first mini-outburst, both at  $L \approx 3 \times 10^{37}$  erg/s (left and right, respectively).

emission [83].

Pulse phase lags were observed during the bursts in Bursting Pulsar [84, 85]. This could be explained with a change in the shape of accretion column base since the column is probably asymmetric when the magnetic dipole axis is inclined with respect to the rotation axis and the accretion rates are high [33]. This change reflects a change in the inner edge of the accretion disk, but poor statistics did not allow us to see corresponding changes in the PDS.

### 5.3 Power density spectra in different luminosities

#### 5.3.1 Shape

For GRO J1744–28, the overall shape of its PDS in outbursts is shown in Figure 8 and can be described by two bumps with a lower turning point (or ‘valley’) around 5 Hz. The nearly sinusoidal pulsations at 2.14 Hz dominate the power right below the turning point. QPOs are visible around 20, 40 and 60 Hz (see [21, 23]).

The long-term evolution with respect to luminosity and time separates the PDS into different periods marked in Figure 2. Some examples of PDS of quiescent burst cycle

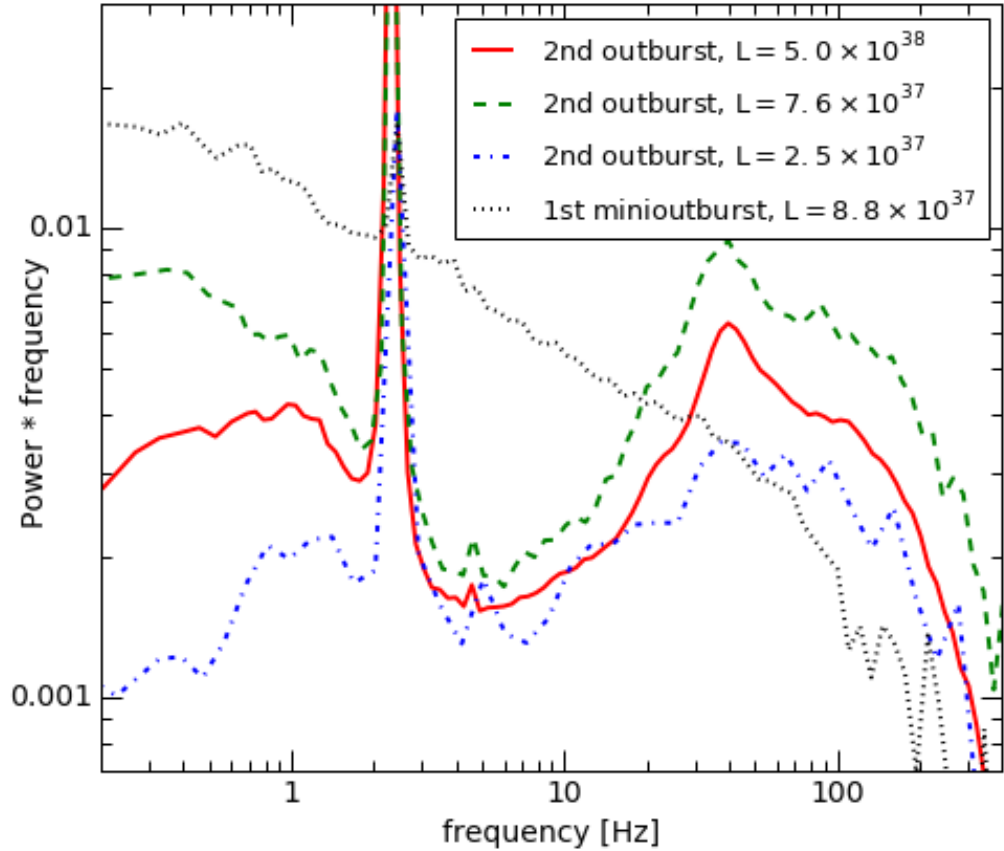


Figure 8. Broadband PDS of quiescent light curve periods during outburst decay and mini-outburst. On the x-axis is the frequency in units of Hertz while the y-axis has rms power times frequency (see section 4.2). The PDS were logarithmically rebinned with respect to frequency to smoothen the noise in the highest frequencies. The dominating regular pulsations are visible around 2 Hz. QPO features are seen as the sharp peak around 20, 40 and 60 Hz. Increased power between 5 and 200 Hz is referred to as the high-frequency ‘bump’.

phase are shown in Figure 8. The shape of the PDS in mini-outbursts is different from the actual outbursts even at the same luminosity above the threshold luminosity for a RPD inner disk: the continuum is a simple power law from low frequencies to an apparent break around 50 Hz; pulsations are less prominent and QPOs are not visible. This may indicate that the actual threshold for the appearance of the RPD inner disk is more difficult to reach when the mass accretion rate increases, but during the decrease of the mass accretion rate, the RPD region remains longer in the inner disk. The increased variability in light curves of mini-outbursts may also be related to this.

The shape of PDS in outbursts also changes on short time scales during the bursting cycle (the periods are described in section 5.1). Burst noise profiles are simple power-laws, but not much can be concluded from those since dead time might smear variability and its effects are impossible to accurately compensate for. The statistics were not good enough for quantifying how the inner regions change in bursts, but high-frequency noise profiles of post-burst periods were similar to the quiescent ones, suggesting a rapid response and return to the pre-burst configuration (RPD disk). Comparing PDS of persistent and post-burst periods in low frequencies indicates that during the bursts, there is a decrease in power that is below 1 Hz. This might be related to mass depletion from the disk causing the bursts and subsequent transformation of the disk structure. A thinner disk would have reduced viscous frequencies and thus more effective damping of noise as discussed above. Also, the post-burst PDS started to lose low-frequency noise at higher luminosities than the quiescent PDS. This may be related to the size of the RPD part of the disk.

When the conditions in the accretion disk change, one expects the shape of the PDS to change accordingly. The viscous properties of the disk are described using the kinematic viscosity  $\nu$ , which is a function of radius only in the case of stable accretion. According to Mushtukov *et al.* (in preparation) specially for  $\alpha$  disks, where gas pressure and Kramer opacity dominate,  $\nu \propto R^{3/4}$ . At high mass accretion rates, however, we expect to see a RPD inner disk instead of a GPD disk (see section 3.2). As discussed in section 3.1, the geometrical thickness of the disk increases in the RPD region. The thickness can be taken to be independent of the radial coordinate. Because viscosity  $\nu \propto (H/R)^2$ , the viscous timescales will decrease in the inner RPD disk. This means that there is less suppression of power on higher frequencies and an additional unsuppressed component, a high-frequency bump, will appear in the noise profile. This can be tested numerically.

Noise profile can be calculated in more detail using the equation for viscous diffusion

$$\frac{\partial \Sigma(R, t)}{\partial t} = \frac{1}{R} \frac{\partial}{\partial R} \left[ R^{1/2} \frac{\partial}{\partial R} (3\nu \Sigma R^{1/2}) \right], \quad (12)$$

where  $\Sigma$  is the local surface density on the disk and Newtonian potential is used (valid for truncated accretion disks) [31]. If viscosity  $\nu$  is a function of radius only, the equation (12) will become linear and its solutions are given by Green's function  $G(R, R', t)$  and depend on the boundary conditions at inner and outer disk radii,  $R_{\text{in}}$  and  $R_{\text{out}}$ . The PDS of the mass accretion rate fluctuation at inner radius is given by  $\bar{G}(R, R', f)$  corresponding to the Green's function solution in the frequency domain. PDS results from the integral:

$$S_{\dot{m}}(R, f) \simeq \int_{R_{\text{in}}}^{R_{\text{out}}} \frac{dR'}{(R')^2} \Delta R(R') |\bar{G}(R, R', f)|^2 S_a(R', f), \quad (13)$$

where  $S_{\dot{m}}(R, f)$  and  $S_a(R, f)$  are the PDS of mass accretion rate variability and initial perturbations at radius  $R$  and  $\Delta R(R')$  is the radius scale where initial perturbations can be considered as coherent ones (close to the local disk scale height  $H$ , see [86]). The Green's functions used in the calculation were derived by Tanaka (2011) [87] for an accretion disk of fixed inner radius and zero torque at the inner boundary. The initial perturbations of the mass accretion rate are described by a zero-centred Lorentzian distribution breaking at the local Keplerian frequency. The rms of initial perturbations is taken to be constant everywhere in the disk.

Some PDS of a disk with a RPD inner region were modeled by Alexander Mushtukov for Mönkkönen *et al.* (in preparation) and are shown in Figure 9. These were done for different sizes of RPD region while the inner radius was kept constant. The models reveal that the variability is completely dominated by the RPD inner disk and that there are two components of power: a bump with roughly a constant height at high frequencies and a bump at low frequencies that depends strongly on the size of the RPD region. If we compare the shapes to the observed ones (see Figure 8), we see that the model provides a very good qualitative match. The observed noise at low frequencies, below the neutron star rotation frequency, comes from the RPD region which extends to radii outside the corotation radius as seen in the schematic of Figure 3. As the 'valley' in the model appears at the viscous frequency, we can see that it should have a value close to 5 Hz. Comparing the modeled spectra to the observed ones in different luminosities may reveal

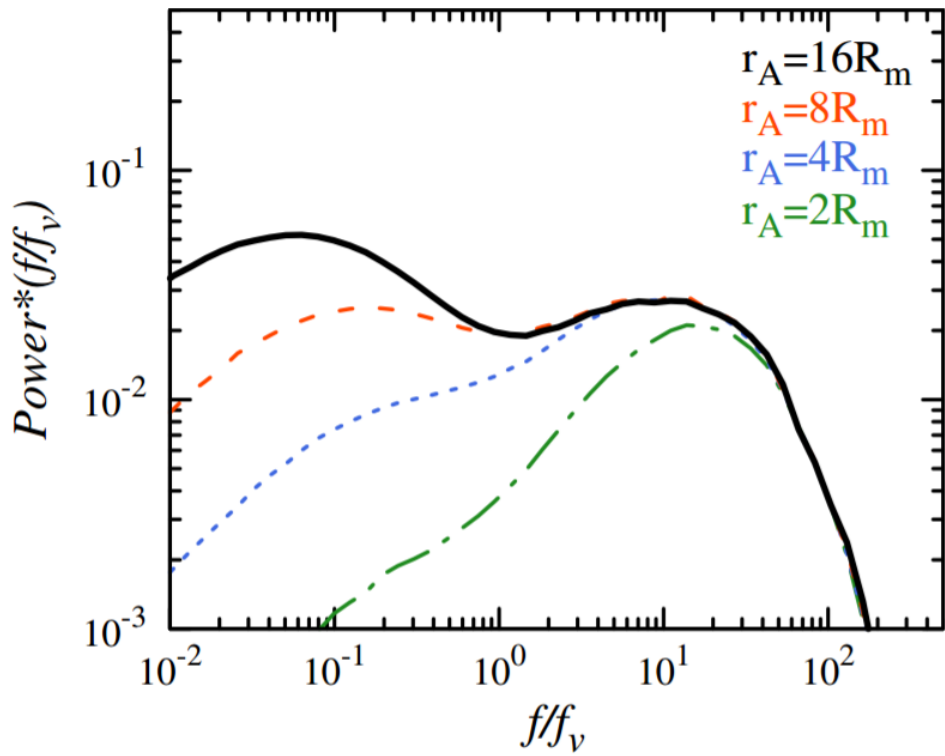


Figure 9. PDS modeled for a disk with constant inner radius but a RPD zone with outer radius  $r_A$ . Power multiplied by frequency is plotted against frequency normalized to viscous frequency at the inner radius. From equation (5) we see that the zone size increases with luminosity so the different sizes correspond to different luminosities. For comparison with observed PDS, see Figure 8.

some additional information about the size evolution of the RPD disk. The modelled PDS have a constant inner radius so from the constant high-frequency edge of the bump we can see that there is no added noise above Keplerian frequencies of the inner radius. Thus we may assume to have the break frequency correspond to the Keplerian frequency of the inner radius even in the RPD part of the disk.

### 5.3.2 Break frequency and QPOs

PDS of GRO J1744–28 have varying shapes, but can be fit with a kink profile

$$p = \frac{c(f/f_b)^a}{((f/f_b)^{2(a-b)} + 1)^{1/2}}, \quad (14)$$

where  $f$  is frequency variable,  $f_b$  is the break frequency,  $a$  is the exponent of the first slope,  $b$  is the exponent of the second slope and  $c$  is the scaling constant (see [60]). In the outbursts, three Lorentzian curves were summed over the kink profile to account for the QPOs

$$p_{\text{QPO}} = \frac{k}{(f - f_{\text{QPO}})^2 + (w/2)^2}, \quad (15)$$

where  $k$  is a scaling constant,  $f_{\text{QPO}}$  is the QPO centroid frequency and  $w$  is the QPO width. Since we were interested in the locations of the QPO centroids, we fixed the widths for each individual QPO to their average values. The quality of the fit is shown in Figure 10.

The break frequency is one of the free parameters in the fit conducted with `curve_fit` function (non-linear least squares) of `scipy.optimize` package for Python. Figure 11 shows the results of how  $f_b$  frequency depends on the luminosity. The errors in frequencies were returned by the fitting function while the errors in luminosity come from the limits of luminosity ranges, and the point in luminosity corresponds to the average of each range. Some data points at low luminosities were left out due to poor statistics.

The fit to break frequencies against luminosity was done for a relation  $f = CL^a$  with  $a$  fixed to 0 or 3/7 or letting  $a$  to vary freely. Only errors in break frequencies were considered for these fits. The reduced  $\chi^2$  for the fits were 2.1, 5.1 and 0.65 after removing scattered data points with initially poor statistics. The best fit was thus achieved with the

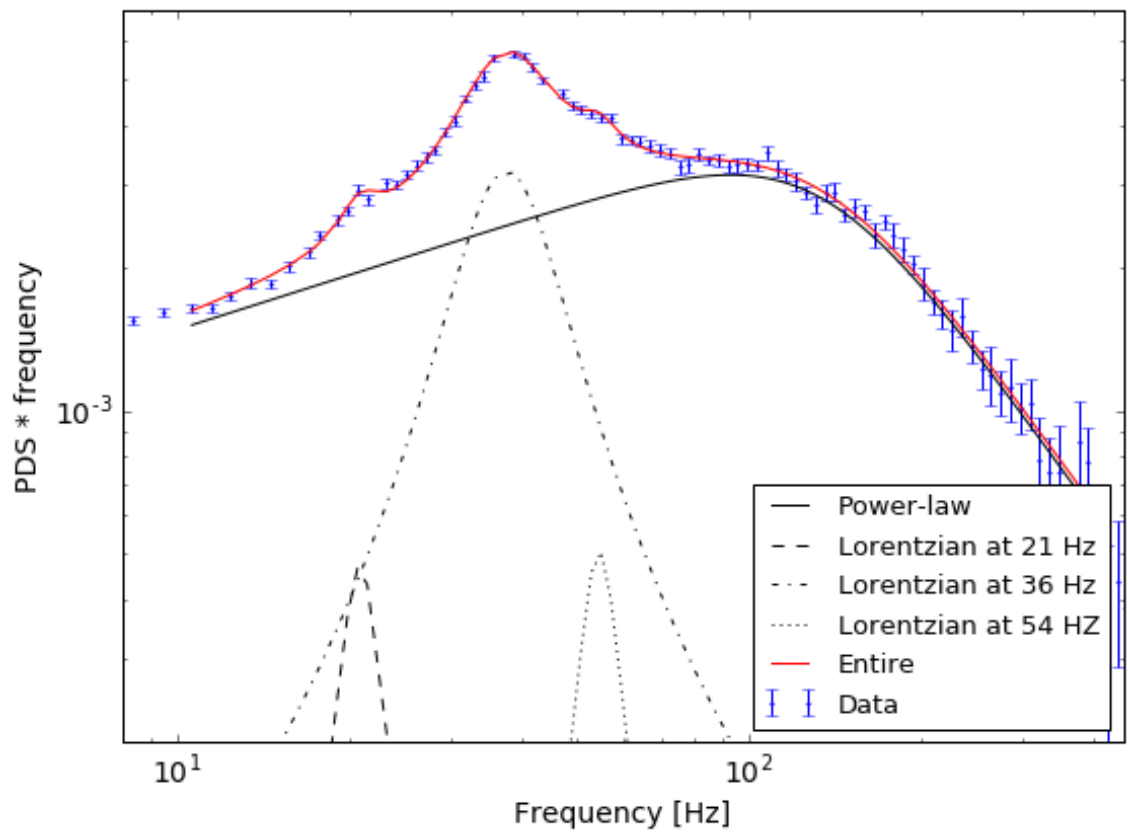


Figure 10. A model (red line) was fit to the data (blue dots with errorbars) in a frequency range from 10 to 400 Hz. The components of the model are shown: a kink profile with smooth black line and three Lorentzian components with dashed, dot-dashed and dotted lines.

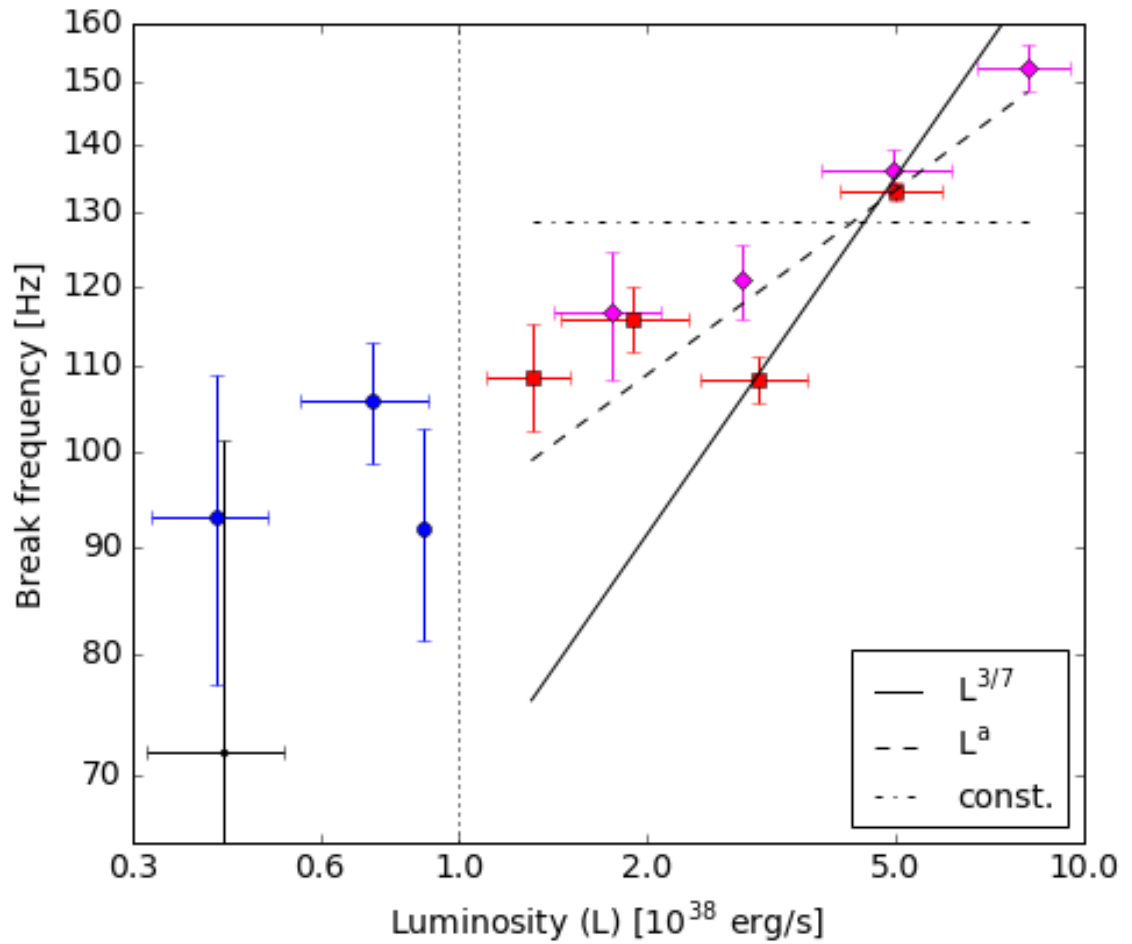


Figure 11. Break frequencies from fits to high-frequency parts of PDS in both outbursts and mini-outbursts plotted against corresponding luminosities. Vertical dotted line separates the outburst data points from the mini-outburst data points: magenta diamonds correspond to the first outburst and red squares to the second outburst while mini-outburst data is given as blue circles and black dots. Fits of luminosity dependencies to break frequencies in the outbursts are shown with the scaling constant being a free parameter.

free exponent, which returned  $a = 0.22 \pm 0.03$ . This value matches the theoretical prediction of 0.23 for a one-temperature optically thick disk dominated by radiation pressure [38, 61]. To test the validity of this result we try to take into account the errors in luminosity and fit the luminosities as a function of break frequency. We get an exponent  $\approx 5.1 \pm 0.5$  (with  $\chi^2 \approx 0.28$ ) which in the original relation corresponds to  $a$  between  $0.18 - 0.22$ , that is, to a very consistent value.

From fits to the PDS, we also get information about the QPOs and their luminosity-dependency. There is no strong correlation between luminosity and QPO location as was found earlier in [21]. QPO cannot be the beat between the Keplerian frequency of the inner disk radius and the NS rotation frequency because the centroid frequencies of the QPOs are not related to the break frequencies in a consistent way: in the first outburst decay, the centroid frequency increases when the luminosity decreases, while in the second outburst decay, the centroid frequency decreases. Possible other causes for QPOs are discussed in section 3.3, but none of them properly explain the attested behaviour.

### 5.3.3 Inner radius

The break frequencies found in previous section can be taken as the Keplerian frequencies of the innermost orbit. Using equation (2), the break frequency of 150 Hz in the highest luminosities corresponds to a radius of only  $6 \times 10^6$  cm. The only assumptions made are the Keplerianity of the disk flow and the mass of the NS,  $M_{\text{NS}} = 1.4M_{\odot}$ . If the maximal frequencies are sub-Keplerian, the actual inner radius is even smaller ( $\approx 10$  per cent discrepancy). This means that during the peak of the outburst, the inner radius would be only five to six times the NS radius. Although deviations from Newtonian potential are still small, at this point, the radiation pressure from the central object should be high and affect the disk [36]. This small value of the inner radius might result from a combination of a small  $\xi$  and a weak dipole component of the magnetic field. Using equation (7) with a magnetic field strength of  $6 \times 10^{11}$  G,  $\xi$  should have a value of 0.3 at the maximal

luminosities of  $1 \times 10^{39}$  erg/s. The dependency of the break frequency on the luminosity implies that  $\xi$  is a function of mass accretion rate (see also [36]).

The dependency of the inner radius on the luminosity is as predicted by Ghosh & Lamb (1992) [38] for a RPD disk as seen in Figure 12. Fitting the standard model for magnetospheric radius (see equation (7)) to the inner radii gives  $B \approx 8 \times 10^9$  G for  $\xi = 0.3$  with reduced  $\chi^2 = 1.2$ , and Ghosh & Lamb (1992) model for RPD disk (see equation (9) and Table 1) gives  $B = (3.08 \pm 0.03) \times 10^9$  G but with reduced  $\chi^2 = 0.17$ . However, as discussed, their model has been criticised for having a too high diffusivity. A reduced dependency of the Keplerian frequency of the innermost orbit on the mass accretion rate can also be found if the star has magnetic multipole moments. For a quadrupolar field we have  $\nu_K \propto \dot{M}^{0.2}$  (see [61]), which also matches the seen behaviour quite well. Although a weaker dipole component and stronger multipoles would explain how the inner radius can get so close to the star and possibly the low pulse fractions, the picture is not fully supported by the sinusoidal pulse profiles. Simulations of hotspots in multipole fields suggest that pulse profiles would differ from purely sinusoidal ones [88].

The inner radius has been derived in other works as well. D'Aí *et al.* (2015) [5] use spectral fitting and get a lower limit for the value of the inner radius,  $2 \times 10^7$  cm, from disk emission and reflection components. They mention that this implies a low  $\xi$  (ratio of magnetospheric radius to Alfvén radius) with a value of 0.2. Younes *et al.* (2015) [89] use the blackbody component with  $kT \approx 0.6$  keV in their spectra to derive the size of the inner reprocessing region. They assume a color correction (or hardness) factor for the disk atmosphere to have a value of  $f_c = 1.8$  and using it find  $R_{\text{in}} = (4 \pm 1) \times 10^7$  cm. Their result for the inner radius derived from a 6.7 keV broadened iron line feature is also consistent with this.

Degenaar *et al.* (2014) [28] used the same 6.7 keV iron feature to derive a similar inner radius of  $2 \times 10^7$  cm. When deriving the magnetic field strength from this, they made assumptions after Cackett *et al.* (2009) [90] and Ibragimov & Poutanen (2009) [91] that

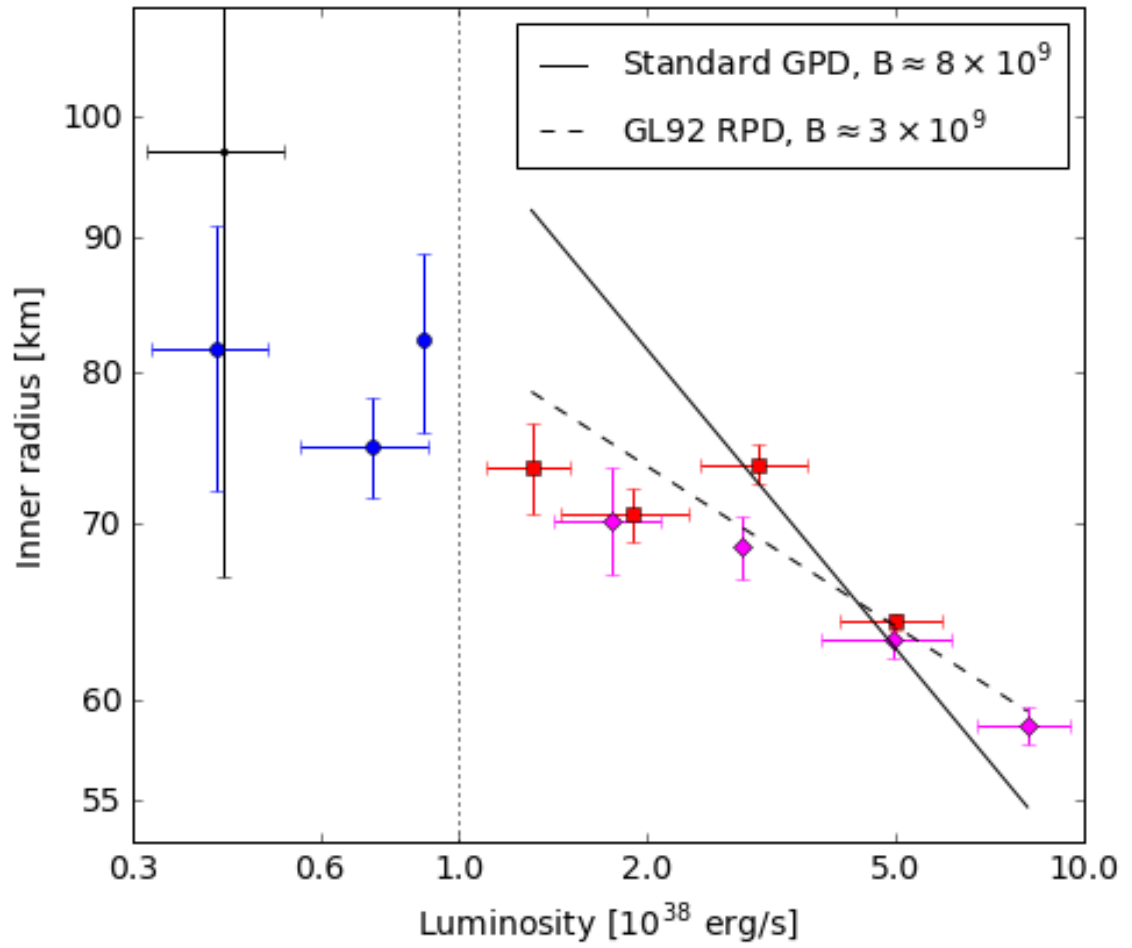


Figure 12. Inner radii corresponding to break frequencies in Figure 11. Theoretical models for standard gas-pressure dominated (GPD) disk and Ghosh & Lamb (1992) [38] radiation-pressure dominated (RPD) disk are fit to the data, and best-fit magnetic field strengths are given.

the emitting region is an accretion mound, while in Bursting Pulsar we expect to see an accretion column with a different emission pattern. They also got a very high inclination ( 50 deg) from their spectral fit, which is not supported by theoretical considerations about the binary evolution [27] and sinusoidal pulse profile [15]. Especially an existence of an accretion column and therefore a radiation source high above the surface should constrain the inclination, if the emission is not reprocessed by an optically thick envelope as in [37]. All in all, it should be taken into account that a RPD inner disk might affect the spectral properties like reflection, because the disk thickness and optical thickness are different than in a standard GPD disk [35].

## 6 Summary

Accreting highly magnetized NSs work as Nature's own laboratories. The interaction of matter and radiation in extreme magnetic fields can be examined through spectral and temporal analysis of X-ray observations.

High-time resolution data provided by *RXTE* has been used for a thorough investigation of variability in X-ray light curves of GRO J1744–28. The uniqueness of this peculiar Bursting Pulsar seems to extend also to the high-frequency variability. Instead of a standard broken power law for standard accretion disks, we see a high-frequency bump in the PDS. The perturbation propagation model of Lyubarskii (1997) [6] can naturally explain the broken power law, but additional work was required to explain the behaviour in this source. It turns out that the shape of the noise profile can be explained if the disk has a RPD inner region.

Super-Eddington luminosities and relatively low magnetic field strength of Bursting Pulsar indeed imply that the inner part of the accretion disk becomes RPD during its outbursts. This is supported by the unique bursting behaviour seen only above some threshold luminosity since burst profiles of type II bursts were successfully modelled as a viscous instability in the RPD inner disk [73].

The PDS can also be used to infer the location of the inner disk radius. In the perturbation propagation model, the break in the noise corresponds to the Keplerian frequency of the inner radius of the accretion disk. This value measures the size of the magnetosphere and can shed light on the interaction between the disk and the magnetosphere. For Bursting Pulsar, the dependency of the break frequency on luminosity does not follow a standard  $L^{3/7}$  relation but follows a different dependency of  $L^{0.23}$ , which according to the model of Ghosh & Lamb (1992) [38] imply a RPD inner disk. The inner radius estimates show that the disk comes very close to the NS, reaching only four to five NS radii from the surface. Together these findings imply that the  $\xi$  parameter has a low value and that it is a function of the mass accretion rate. Thus it has been once again shown that observational evidence is crucial for the development of models, and further work is required to reveal what is actually happening in GRO J1744–28.

## References

- [1] J. E. Pringle & M. J. Rees, *Astronomy and Astrophysics* **21**, (1972).
- [2] D. Lai, *EPJ Web of Conferences* **64**, 1 (2014).
- [3] J. Ross *et al.*, *Monthly Notices of the Royal Astronomical Society* **468**, (2017).
- [4] A. R. King *et al.*, *Physics Today*, 3rd ed. (Cambridge University Press, , 2002), Vol. 39, p. 384.
- [5] A. D’Aí *et al.*, *Monthly Notices of the Royal Astronomical Society* **449**, 4288 (2015).
- [6] Y. E. Lyubarskii, *Monthly Notices of the Royal Astronomical Society* **292**, 679 (1997).
- [7] R. Doroshenko *et al.*, *Monthly Notices of the Royal Astronomical Society* **452**, 2490 (2015).
- [8] J. M. Lattimer & M. Prakash, *Science* **304**, 536 (2004).
- [9] V. S. Beskin *et al.*, *Space Science Reviews* **191**, 1 (2015).
- [10] E. van den Heuvel, in *NATO Advanced Research Workshop on X-Ray Binaries and the Formation of Binary and Millisecond Radio Pulsars*, edited by E. P. J. van den Heuvel & S. A. Rappaport (Springer, Santa Barbara, CA, USA, 1992), p. 233.
- [11] N. I. Shakura & R. A. Sunyaev, *Astronomy and Astrophysics* **24**, 337 (1973).
- [12] M. Revnivtsev & S. Mereghetti, *Space Science Reviews* **191**, 293 (2015).
- [13] G. J. Fishman *et al.*, *International Astronomical Union Circular* **6272**, (1995).
- [14] C. Kouveliotou *et al.*, *Nature* **379**, L799 (1996).
- [15] M. H. Finger *et al.*, *Nature* **381**, L291 (1996).
- [16] S. Y. Sazonov *et al.*, *Astronomy Letters*, Volume 23, Issue 3, May 1997, pp.286-292; *Pis'ma v Astronomicheskii Zhurnal*, Vol. 23, p. 326 **23**, 286 (1997).
- [17] A. B. Giles *et al.*, *The Astrophysical Journal* **469**, L25 (1996).
- [18] M. J. Stark *et al.*, in *AIP Conference Proceedings* (AIP, , 1998), pp. 401–404.
- [19] J. Cannizzo, *The Astrophysical Journal Letters* **466**, L31 (1996).
- [20] A. P. Lightman & D. M. Eardley, *The Astrophysical Journal* **187**, L1 (1974).
- [21] W. Zhang *et al.*, *The Astrophysical Journal* **469**, L29 (1996).
- [22] M. A. Alpar & J. Shaham, *Nature* **316**, 239 (1985).

- [23] J. M. Kommers *et al.*, *The Astrophysical Journal* **482**, L53 (1997).
- [24] T. Dotani *et al.*, *International Astronomical Union Circular* **6337**, (1996).
- [25] M. Nishiuchi *et al.*, *The Astrophysical Journal* **517**, 436 (1999).
- [26] W. Cui, *The Astrophysical Journal* **482**, L163 (1997).
- [27] S. Rappaport & P. C. Joss, *The Astrophysical Journal* **486**, 435 (1997).
- [28] N. Degenaar *et al.*, *The Astrophysical Journal* **796**, L9 (2014).
- [29] I. A. Mereminskiy *et al.*, ATel #10073: The new X-ray outburst of GRO J1744-28 detected with INTEGRAL, 2017.
- [30] T. Russell *et al.*, ATel #10106: Radio luminosity upper limits of the transient neutron star low-mass X-ray binary GRO J1744-28, 2017.
- [31] J. E. Pringle, *Annual Review of Astronomy and Astrophysics* **19**, 137 (1981).
- [32] S. A. Balbus & J. F. Hawley, *The Astrophysical Journal* **376**, 214 (1991).
- [33] M. M. Basko & R. A. Sunyaev, *Monthly Notices of the Royal Astronomical Society* **175**, 395 (1976).
- [34] A. A. Mushtukov *et al.*, *Monthly Notices of the Royal Astronomical Society* **454**, 2539 (2015).
- [35] V. F. Suleimanov *et al.*, *Astronomy Reports* **51**, 549 (2007).
- [36] A. Chashkina *et al.*, eprint arXiv:1703.07005 (2017).
- [37] A. A. Mushtukov *et al.*, *Monthly Notices of the Royal Astronomical Society* **467**, 1202 (2016).
- [38] P. Ghosh & F. K. Lamb, in *NATO Advanced Research Workshop on X-Ray Binaries and the Formation of Binary and Millisecond Radio Pulsars*, edited by E. P. J. van den Heuvel & S. A. Rappaport (Springer, Santa Barbara, CA, USA, 1992), Chap. 8, pp. 487–510.
- [39] A. F. Illarionov & R. A. Sunyaev, *Astronomy and Astrophysics* **39**, 185 (1975).
- [40] S. S. Tsygankov *et al.*, *A&A* **593**, 1 (2016).
- [41] F. K. Lamb *et al.*, *Astrophysical Journal* **184**, 271 (1973).
- [42] P. Ghosh & F. K. Lamb, *The Astrophysical Journal* **232**, 259 (1979).
- [43] P. Ghosh & F. K. Lamb, *Astrophysical Journal* **223**, L83 (1978).
- [44] Y. M. Wang, *The Astrophysical Journal* **449**, L153 (1995).

- [45] N. E. White & L. Stella, *Monthly Notices of the Royal Astronomical Society* **231**, 325 (1988).
- [46] J. J. Aly & J. Kuijpers, *Flaring interactions between accretion disk and neutron star magnetosphere*, 1990.
- [47] W. Kluźniak & S. Rappaport, *Astrophysical Journal* **671**, 1990 (2007).
- [48] L. Bildsten *et al.*, *The Astrophysical Journal Supplement Series* **113**, 367 (1997).
- [49] A. Sanna *et al.*, eprint arXiv:1703.04449 (2017).
- [50] F. Shu *et al.*, *The Astrophysical Journal* **429**, 781 (1994).
- [51] R. V. E. Lovelace *et al.*, *Monthly Notices of the Royal Astronomical Society* **275**, 244 (1995).
- [52] S. Matt & R. E. Pudritz, *The Astrophysical Journal* **632**, L135 (2005).
- [53] D. Lai, *Physics in Very Strong Magnetic Fields*, 2015.
- [54] C. G. Campbell, *Monthly Notices of the Royal Astronomical Society* **403**, 1339 (2010).
- [55] C. Terquem & J. C. B. Papaloizou, *Astron. Astrophys* **360**, 1031 (2000).
- [56] A. R. King *et al.*, *Monthly Notices of the Royal Astronomical Society* **348**, 111 (2004).
- [57] E. Churazov *et al.*, *Monthly Notices of the Royal Astronomical Society* **321**, 759 (2001).
- [58] O. Kotov *et al.*, *Monthly Notices of the Royal Astronomical Society* **327**, 799 (2001).
- [59] P. Arévalo & P. Uttley, *Monthly Notices of the Royal Astronomical Society* **367**, 801 (2006).
- [60] M. Revnivtsev *et al.*, *Astronomy and Astrophysics* **507**, 1211 (2009).
- [61] D. Psaltis & D. Chakrabarty, *The Astrophysical Journal* **521**, 332 (1999).
- [62] M. G. Revnivtsev *et al.*, *MNRAS* **451**, 4253 (2015).
- [63] M. van der Klis, *Advances in Space Research* **22**, 925 (1998).
- [64] R. I. Klein *et al.*, *The Astrophysical Journal* **469**, L119 (1996).
- [65] V. Rezania & J. C. Samson, *Astronomy and Astrophysics* **436**, 999 (2005).
- [66] N. I. Shakura & R. A. Sunyaev, *Monthly Notices of the Royal Astronomical Society* **175**, 613 (1976).

- [67] X.-D. Li & E. van den Heuvel, *Astronomy and Astrophysics* **321**, L25 (1997).
- [68] R. E. Taam & R. E. Picklum, *The Astrophysical Journal* **224**, 210 (1978).
- [69] P. C. Joss & F. K. Li, *The Astrophysical Journal* **238**, 287 (1980).
- [70] K. Jahoda *et al.*, in *The Active X-ray Sky: Results from BeppoSAX and RXTE* (PUBLISHER, , 1997), p. 210.
- [71] R. E. Taam & D. N. C. Lin, *The Astrophysical Journal* **287**, 761 (1984).
- [72] J. P. Lasota & D. Pelat, *Astronomy and Astrophysics* **249**, 574 (1991).
- [73] J. K. Cannizzo, *The Astrophysical Journal* **482**, 178 (1997).
- [74] C. A. Glasser *et al.*, *IEEE Transactions on Nuclear Science* **41**, 1343 (1994).
- [75] A. Giles *et al.*, *Publications of the Astronomical Society of Australia* **12**, 219 (1995).
- [76] B. K. Irby, HEASoft, <https://heasarc.nasa.gov/lheasoft/>, accessed April 28, 2017.
- [77] XTE help desk, RXTE GOF: Answers to FAQ, [https://heasarc.gsfc.nasa.gov/docs/xte/ftools/xtefaq\\_answers.html](https://heasarc.gsfc.nasa.gov/docs/xte/ftools/xtefaq_answers.html), accessed May 3, 2017.
- [78] D. A. Leahy *et al.*, *Astrophysical Journal* **266**, 160 (1983).
- [79] S. Miyamoto *et al.*, *The Astrophysical Journal* **383**, 784 (1991).
- [80] M. M. Romanova *et al.*, *Advances in Space Research* **38**, 2887 (2006).
- [81] Y. E. Lyubarskii & R. A. Sunyaev, *Soviet Astronomy Letters* **14**, (1988).
- [82] J. Poutanen *et al.*, *The Astrophysical Journal* **777**, 115 (2013).
- [83] A. A. Lutovinov *et al.*, *Monthly Notices of the Royal Astronomical Society* **448**, 2175 (2015).
- [84] M. J. Stark *et al.*, *The Astrophysical Journal* **470**, L109 (1996).
- [85] A. D'Aí *et al.*, *Monthly Notices of the Royal Astronomical Society: Letters* **463**, L84 (2016).
- [86] J. D. Hogg & C. S. Reynolds, *The Astrophysical Journal* **826**, (2016).
- [87] T. Tanaka, *Monthly Notices of the Royal Astronomical Society* **410**, 1007 (2011).
- [88] M. Long *et al.*, *Monthly Notices of the Royal Astronomical Society* **374**, 436 (2006).
- [89] G. Younes *et al.*, *The Astrophysical Journal* **804**, 43 (2015).
- [90] E. M. Cackett *et al.*, *The Astrophysical Journal* **694**, L21 (2009).
- [91] A. Ibragimov & J. Poutanen, *Monthly Notices of the Royal Astronomical Society* **400**, 492 (2009).